Review of Scientific Instruments | ARTICLE | scitation.org/journal/rsi

Cinematic reflectometry using QIKR, the quite intense kinetics reflectometer

Cite as: Rev. Sci. Instrum. 94, 013302 (2023); doi: 10.1063/5.0122279
Submitted: 23 August 2022 • Accepted: 14 November 2022 •
Published Online: 4 January 2023

View Online Export Citation CrossMark

J. F. Ankner,[1,a)] R. Ashkar,[2] J. F. Browning,[3] T. R. Charlton,[3] M. Doucet,[3] C. E. Halbert,[3] F. Islam,[4] A. Karim,[5] E. Kharlampieva,[6] S. M. Kilbey II,[7] J. Y. Y. Lin,[1] M. D. Phan,[3,8] G. S. Smith,[3,b)] S. A. Sukhishvili,[9] R. Thermer,[1] G. M. Veith,[10] E. B. Watkins,[3,11] and D. Wilson[1]

AFFILIATIONS

[1]Second Target Station Project, Oak Ridge National Laboratory, Oak Ridge, Tennessee 37831, USA
[2]Department of Physics, Virginia Tech, Blacksburg, Virginia 24061, USA
[3]Neutron Sciences Division, Oak Ridge National Laboratory, Oak Ridge, Tennessee 37831, USA
[4]Neutron Technologies Division, Oak Ridge National Laboratory, Oak Ridge, Tennessee 37831, USA
[5]Department of Chemical and Biomolecular Engineering, University of Houston, Houston, Texas 77204, USA
[6]Department of Chemistry, University of Alabama at Birmingham, Birmingham, Alabama 35294, USA
[7]Department of Chemistry, University of Tennessee, Knoxville, Tennessee 37996, USA
[8]Department of Chemical and Biomolecular Engineering, University of Delaware, Newark, Delaware 19716, USA
[9]Department of Materials Science and Engineering, Texas A&M University, College Station, Texas 77843, USA
[10]Chemical Sciences Division, Oak Ridge National Laboratory, Oak Ridge, Tennessee 37831, USA
[11]Physics Division, Los Alamos National Laboratory, Los Alamos, New Mexico 87545, USA

Note: Paper published as part of the Special Topic on New Science Opportunities at the Spallation Neutron Source Second Target Station.
[a)]**Author to whom correspondence should be addressed:** anknerjf@ornl.gov
[b)]Retired.

ABSTRACT

The Quite Intense Kinetics Reflectometer (QIKR) will be a general-purpose, horizontal-sample-surface neutron reflectometer. Reflectometers measure the proportion of an incident probe beam reflected from a surface as a function of wavevector (momentum) transfer to infer the distribution and composition of matter near an interface. The unique scattering properties of neutrons make this technique especially useful in the study of soft matter, biomaterials, and materials used in energy storage. Exploiting the increased brilliance of the Spallation Neutron Source Second Target Station, QIKR will collect specular and off-specular reflectivity data faster than the best existing such machines. It will often be possible to collect complete specular reflectivity curves using a single instrument setting, enabling "cinematic" operation, wherein the user turns on the instrument and "films" the sample. Samples in time-dependent environments (e.g., temperature, electrochemical, or undergoing chemical alteration) will be observed in real time, in favorable cases with frame rates as fast as 1 Hz. Cinematic data acquisition promises to make time-dependent measurements routine, with time resolution specified during post-experiment data analysis. This capability will be deployed to observe such processes as *in situ* polymer diffusion, battery electrode charge–discharge cycles, hysteresis loops, and membrane protein insertion into lipid layers.

SCIENCE DRIVERS

General

Interfaces are ubiquitous and the transport of atoms, molecules, or charge across interfaces is fundamentally important to the properties and function of materials. Interfacial potential energy gradients drive a host of thermodynamic processes. Many advanced properties sought through materials by design will only be realized in new materials having at least one nanoscale dimension. In these systems, new functionality can arise from surface-dominated forces and interactions, rather than from the less-specific interactions that span the bulk. Neutron reflectometry directly probes air/solid, solid/liquid, air/liquid, and liquid/liquid interfaces. The Quite Intense Kinetics Reflectometer (QIKR) is designed to shine the unprecedented brightness of the Second Target Station (STS) onto these problems.

The ability to perform time-resolved studies with the unique capabilities that neutron beams offer is one of the most important advances enabled by the STS. Structural alterations that follow changes in temperature, shear, pressure, and other environmental conditions are vital to the performance and processing of materials. Many of these interesting structural processes occur over seconds to minutes after the stimulus, which is well matched to the new capabilities afforded by the STS. In favorable cases, the potential for resolving materials changes with each neutron pulse may exist and, hence, time-resolved experiments (~100 ms) become feasible.

A recent report describes the science to be addressed by the STS (ORNL, 2019). Drawn from this and other sources, the following brief survey illustrates the wide range of topics addressable by a high-intensity broad bandwidth reflectometer like QIKR.

Soft matter

Soft matter encompasses materials that are at least 1000 times mechanically weaker than conventional solids. Soft matter is typically composed of large molecules, polymers, membranes, colloidal suspensions, or foams, and also encompasses dislocations and grain-boundary networks. Common examples include plastics, detergents, oils, gels, pastes, paints, and condiments. There is strong overlap and synergy between soft matter and biological materials.

Polymer molecules located at solid and fluid interfaces exhibit an enormous spectrum of technological applications. For example, they provide a mechanism for imparting colloidal stabilization, are used as protective coatings (including the mechanical protection of hard materials against friction and wear), govern the interactions of biological cells with surfaces, and through judicious design are used to modulate dispersion properties (e.g., rheology) under a variety of processing conditions (Stockton and Rubner, 1997). Knowledge of the conformations that adsorbed or terminally anchored chain molecules adopt when subjected to confinement and/or solvent flow is essential for predicting the interaction forces and tribological and rheological properties in materials utilizing thin-film technologies (Sanchez, 2013).

Processes occurring at liquid/liquid interfaces are relevant across a broad range of scientific disciplines, from chemical extraction to metabolic processes at biological and synthetic membranes (Schlossman, 2002). These interfaces are difficult to interrogate, but the penetrating power of neutrons and their sensitivity to light elements provide a unique capability.

Solvent extraction plays a major role in the hydrometallurgical separation of base and precious metals, such as rare earths (Tasker *et al.*, 2004), as well as in the reprocessing of spent nuclear fuel and in the separation and isolation of long-lived radionuclides from high-level nuclear waste (Nash, 2006). Solvent extraction is a flexible and scalable technique based on the distribution of chemical species between two immiscible liquids, usually an aqueous phase in contact with an organic phase. Although the interaction of metal ions with aqueous complexants and organic extractants at the aqueous–organic interface determines the efficiency and kinetics of extraction processes, little is known about the molecular complexes that form at the interface or the ion transfer mechanisms that underlie the process of solvent extraction. Neutron reflectometry provides a unique ability to view these interfaces by traversing a liquid phase as the incident medium. Depending on the problem, the transmitting medium may be either above or below the interface, so QIKR is designed to operate in both geometries. Reduced measuring time will allow tracking of interfacial processes on seconds-to-minutes time scales.

The extraction cycle consists of both forward- and back-extraction processes. Of interest for neutron reflectivity experiments is an exploration of the role of aqueous complexants and buffers in the back-extraction process enabled by a liquid/liquid interface cell capable of injection/exchange of various solvent/solute components. Such a cell enables formation of well-defined, planar liquid–liquid interfaces. The kinetics and composition of complexes of ions formed at the interface and their interaction with extracting surfactant molecules can be derived from the measured reflectivity curves.

To address the four cross-cutting National Academy of Engineering Grand Challenges in health, food, energy, and sustainability (NAE, 2022) and the NSF guidelines for Growing Convergence Research (NSF, 2022; Gropp, 2016), interfaces of soft materials and polymers should be designed to be self-cleaning, antifouling (for environmental and energy applications, such as in filtration membranes) (Maan *et al.*, 2020; Zhang *et al.*, 2017; Geyer *et al.*, 2020; and Yan *et al.*, 2020), and adaptable to changing environments and in addition to deliver bioactive molecules in biomedical settings. Yet the fundamentals of constructing such surfaces are not well understood. A specific challenge is to observe the short-term response of surfaces to changing environments (e.g., light- or analyte-triggered dehydration or conformational challenges). This short-term response, often occurring on time scales of seconds or minutes, strongly affects long-term surface antifouling/drug-delivery behavior, but techniques to study such responses are lacking. Time-resolved neutron reflectometry (NR) within controlled sample environments (e.g., shear, contact with adsorbing molecules, application of light) will enable the observation of surface reorganization, inversion of polymer molecules, response of surfaces to invading molecules, and release of active compounds from coatings at relevant time scales and thus will enable the design of surface properties for maximized antifouling/drug-delivery functionality.

Energy materials

Energy storage and conversion are growing in importance for the nation's energy and economic security as described in DOE's Energy Storage Grand Challenge Roadmap (BES, 2022). Focus areas

where QIKR can contribute include, but are not limited to, traditional lithium-ion batteries as well as newer cell chemistries, including sodium ion, metal–air, flow, and all solid-state batteries. There are two fundamental challenges limiting energy storage development: (1) interfacial chemistry and (2) materials assembly.

Challenge 1: Interfacial chemistry

In every single energy storage system, interfacial reactions dominate cell performance and lifetime. These reactions occur because of large oxidation and reduction potentials at the cathode and anode, respectively, causing the decomposition of materials at the electrode surface (Peled, 1979; Peled and Menkin, 2017). These decomposition reaction products are described as the solid electrolyte interphase (SEI) at the anode and the cathode electrolyte interphase (CEI) at the positive electrode (Verma *et al.*, 2010). These reactions lead to mixtures of inorganic (e.g., LiF, Li_2O, Li_2S, Li_3N) and organic/polymeric compounds (e.g., Li–R–O–CO_2, alkoxides, ethers) and depend on cell chemistry, electrolyte, cell additives, and the chemical potential of the interface. A poorly formed SEI can lead to cell failure and safety issues such as ignition and outgassing. Most current understanding of these processes derives from *ex situ* characterization using infrared- and vacuum-based scattering methods from cells disassembled and washed prior to analysis. Given that the SEI and CEI mediate battery stability, ion transport, cell power, and lifetime, it is essential to develop a predictive understanding of their chemistry.

In situ neutron reflectometry measurements over the past decade have provided previously unobtainable insights into SEI and CEI chemistry. Reflectivity data have revealed the spontaneous segregation of solvent and ions at anode and cathode surfaces, resulting in a 3–5 nm-thick interface layer with liquid electrolytes. These films are thicker than the classic double layer and are believed to be the first steps of SEI formation (Veith *et al.*, 2014). Upon lithium-ion cycling, it has been determined that interfaces on silicon anodes are highly dynamic and change in thickness and composition with the state of charge in a process called "breathing" (Veith *et al.*, 2014; Fears *et al.*, 2016; and Veith *et al.*, 2017). SEIs and CEIs range in thickness from 1 to 100 nm. Furthermore, salt components of the SEI are easily removed by solvent exposure, leaving insoluble species behind, providing a link between *ex situ* and *in situ* characterization (Browning *et al.*, 2019; Browning *et al.*, 2020). Other groups have focused on the diffusion of lithium within an anode and identified phase fronts that form with the amorphization of crystalline silicon (Jerliu *et al.*, 2013; Seidlhofer *et al.*, 2016; Jerliu *et al.*, 2014; and DeCaluwe *et al.*, 2015), the interface chemistry of cathodes (Hirayama *et al.*, 2010; Veith *et al.*, 2015; and Minato *et al.*, 2016), and lithium (Avdeev *et al.*, 2017) or carbon anodes (Kawaura *et al.*, 2020). In all these studies, data were collected in "static" modes where a cell was charged to a specified voltage or lithium content, allowed to relax, and then reflectivity data were collected. This data collection choice was dictated by the speed of available data acquisition parameters, neutron flux, and cell design. However, from these prior studies, chemistry and composition change with the state of charge over time periods ranging from seconds to years.

From the work described above flow several fundamental questions addressable using cinematic reflectivity measurement of classic liquid electrolytes (e.g., 1.2M $LiPF_6$ in mixtures of ethylene carbonate/diethyl carbonate):

- SEI formation: How do the solvent and ions organize and change during the initial cell charging process? How do these rearrangements affect stripping and plating of lithium? What happens at faster or slower rates of charge and cycling?
- SEI dynamics: How does the SEI change upon termination of charging? How do Li ions relax when not under potential? Can we develop ways to improve electrode life by studying nanoscale structural changes with time?
- SEI lifetime: What happens to the interfacial chemistry when the cell suffers from an SEI failure resulting in self-discharge over several hours? Can this phenomenon be controlled? Are there specific electrochemical signals that can be correlated with chemical and structural changes?

Beyond classic liquid electrolytes, there is a growing need to understand interfacial chemistry in solid-state batteries where the electrolyte is a solid ion conductor (e.g., Li–La–Ti–O, Li–La–Ta–Zr–O, Li–P–O–N). In these systems, there is no liquid electrolyte, rendering them safer and longer-lived. However, there are several fundamental questions to be addressed, including the following:

- Lithium metal interface: What happens as lithium metal is plated at the anode–solid electrolyte interface? Are observed chemical changes passivating or constantly changing? What chemical changes lead to lithium orphaning?
- Cathode–solid electrolyte interface: What happens to the solid electrolyte at high oxidation potentials? Do lithium ions segregate at the interface? How do lithium ions move across the interface?

Answers to any of these questions will provide pathways to improved battery performance, which is essential for successful deployment of the next generation of energy storage technologies.

Challenge 2: Materials assembly

Over the last 40 years, and with the explosion of computation methods, virtually all electrode and solid electrolyte materials have been identified. The challenge now is to determine how, precisely and reproducibly, to assemble these materials into structures that are functional. Functionality includes optimized orientation to facilitate lithium transport as well as the interfacial stability discussed above. Candidate materials include lithium-containing ceramics, lithium salts, and lithium metal, in addition to proton-containing polymers and processing solvents. Fundamental questions include the following:

- How do we assemble two dissimilar ceramics without allowing interdiffusion of atoms between them? What happens to the two materials under chemical potential and over time?
- How does the assembly of ion-conducting polymers at ceramic interfaces vary with processing conditions?
- What happens to the interface when lithium metal is deposited or grown on a solid electrolyte?
- How do passivation and sacrificial additives affect the chemistry of the solid electrolyte?

Answering these questions is essential to moving beyond traditional stochastic battery formation processes toward rational design. This science is completely new and requires the ability to track the segregation of Li- and H-containing materials as a function of temperature, pressure, field, and chemical potential with time.

Beyond energy storage

The science discussed above focuses on batteries, but there are numerous other technological areas where understanding changes in buried interfaces with time and state is crucial, including concentrated solar plants, the growth of perovskite solar cells, electrochemical conversion of CO_2 and N_2 into fuels, and supercapacitors. In every case, interfaces change as a function of potential over time in ways that are not understood.

For example, the corrosion of metal alloys determines the lifetime and efficiency of the thermal molten salt systems envisioned for nuclear and solar energy capture and conversion. In these systems, interface chemistry between the molten salt and its containment mediates metal leaching and heat transfer but it is unclear how, or on what time scales, or even what happens with subtle changes in chemistry over time. For perovskite solar cells, how does the current-collector interface with the perovskite evolve over time? How does this chemistry affect cell efficiency? Can this process be directed? Within a supercapacitor, how do ions segregate or change orientation over extended periods of time? In every case, the organization and relaxation of species under potential play a key, and currently unknown, role in determining lifetime and performance. The ability to probe these interface structures as a function of time *in situ* will be essential to developing solutions to the nation's energy security needs.

Biology

Biological and biomimetic membranes are ubiquitous in a variety of research areas at the interface of biology, biophysics, health care, and biotechnology (Young-Rok *et al.*, 2012; Nielsen, 2009; Yingchoncharoen *et al.*, 2016; Peetla *et al.*, 2009; Egrot *et al.*, 2010; and Siontorou *et al.*, 2017). In cells, the intrinsically interfacial nature of plasma membranes makes them the interaction front between the cell and its environment. In addition, cell membranes are the first line of defense against pathogens, e.g., viruses, fungi, and bacteria (Auth *et al.*, 2018). However, despite the central role of membranes in cellular function, very little is known about how they respond to their environment, to viral proteins, and to the bacterial and fungal secretions responsible for cellular hijacking. Furthermore, anomalies in cell membrane composition, structure, and in-plane arrangements have been implicated in various disease conditions, including cancer and multidrug resistance—two imminent threats to global public health (Simons and Ikonen, 1997; Michel and Bakovic, 2007). For instance, growth and clustering of lipid rafts—nanoscopic lipid domains rich in cholesterol—have been linked to the migration and spread of cancerous cells (Bi *et al.*, 2018) and for the stabilization of multidrug-resistant proteins that actively export drugs out of diseased cells (Rockwell, 2013; de Lange, 2007). With the envisioned surge of infectious diseases (Bongomin *et al.*, 2017; Singhal, 2020) and the emergence of various forms of multidrug resistance (Liscovitch and Lavie, 2000), it is more pressing than ever to understand how membranes rearrange under disease conditions, how they interact with pathogens, and how the development of new drugs can effectively control the molecular and nanoscopic arrangements within cell membranes. All these outstanding questions require the ability to (1) probe membranes with high resolution in different environments and in contact with different interfaces, (2) selectively interrogate functional membrane features, and (3) understand how such features evolve over time. Addressing these questions is crucial for (a) the fundamental understanding of the collective response of membranes to molecular and environmental cues, (b) the determination of membrane physical properties responsible for impeding pathogen attack, and (c) the development of membrane-based therapeutic approaches based on experimentally validated molecular design rules.

Investigations of this nature benefit from the selective isotope sensitivity of neutron scattering (Ashkar *et al.*, 2018) and from the molecular- and sub-molecular-level resolution of neutron reflectometry (Majewski *et al.*, 2000; Wong *et al.*, 1999; Majkrzak *et al.*, 2000; and Junghans *et al.*, 2015). Here, it is important to acknowledge that while neutron reflectometry from supported lipid bilayers has been used in a multitude of studies and has shed important light on vital membrane properties (Nanda *et al.*, 2010; Hoogerheide *et al.*, 2017; Benedetto *et al.*, 2014; Luchini *et al.*, 2017; Fragneto-Cusani, 2001; and Gerelli *et al.*, 2012), studies on lipid monolayers at the air–water interface suffer from reflectivity profiles with very few features—rendering model fitting and parameter extraction difficult. However, the combination of reflectometry measurements with molecular dynamics (MD) simulations offers a powerful means of modeling reflectometry data and unraveling the molecular rearrangements inferred from subtle reflectivity changes (McCluskey *et al.*, 2019). In addition to the use of MD simulations to model specular reflectivity from laterally averaged membrane structures, recent developments in simulation capturing in-membrane structures (Dorrell *et al.*, 2020), e.g., raft-like lipid domains (Levental *et al.*, 2020; Simons and Ikonen, 1997), open new possibilities for resolving lateral membrane features of relevance to biological function, disease conditions, and therapeutic approaches. More importantly, the ability to probe the evolution of such features over sub-minute time scales will revolutionize our understanding of membranes as dynamic entities that constantly detect interfacial changes and respond to them in real time. Unfortunately, the current absence of methods that enable a view of "membranes in action" is a bottleneck. Thus, the development of experimental methods that afford a direct view of membrane kinetics is key to unraveling the active face of cell membranes—a topic that is in close alignment with the DOE-BESAC grand challenge, Mastering Hierarchical Architectures and Beyond Equilibrium Matter (Hemminger, 2015), the milestone of engineering biotic and abiotic interfaces identified in the 2021 EBRC Engineering Biology and Materials Science Roadmap (EBRC, 2022), and identified as one of NSF's ten Big Ideas (Gropp, 2016).

Bilayer membranes, composed of inner and outer amphiphilic leaflets, are a defining structural motif in biology. Lipid flip-flop is a biological process in which lipids traverse a bilayer membrane from one leaflet to the other. During flip-flop, polar lipid head groups must translocate across membranes not only to sustain growth but also to support the function of certain biosynthetic pathways,

maintain the membrane's nonrandom asymmetry, contribute to the mechanical stability of the cell, and to manage programmed cell death. Lipids are actively transported across a lipid bilayer by membrane proteins, or flippases, on time scales of seconds or minutes. Flippases also exist in forms that trigger non-bilayer rearrangement or induce transient defects in lipid bilayers. Much work has focused on the thermodynamics of lipid translocation to establish the flipping mechanism and to identify intermediate structures. However, there are discrepancies in the time scale, occurrence, and features of the flip-flop mechanism, depending on the techniques used to characterize it. Neutron reflectometry (NR) possesses a fundamental advantage over techniques that employ modified or labeled lipids, which may differ chemically and structurally from the native lipids found in biological membranes. NR provides the composition of membrane leaflets in the direction normal to the interface, which makes the technique essential in the study of lipid flip-flop systems (Gerelli *et al.*, 2012). QIKR, with greater flux, will be able to capture fast lipid translocation triggered by flippases and to identify the mechanisms of lipid flip-flop systems for the first time.

Medical devices, such as infusion tubes or prefilled syringes, are typically either comprised of hydrophobic polymeric materials or are coated with a layer of hydrophobic oil on a glass surface. Understanding the effect of interfacial rheological forces at hydrophobic surfaces upon adsorption and possible conformational changes of proteins and surfactants is crucial for storage stability and delivery of pharmaceutical liquid formulations (Chi *et al.*, 2003). On a neutron beamline, a rheometer can be used to mimic medical injection processes by rotating a prepared surface past a protein solution. The *in situ* interfacial interactions between hydrophobic coated substrates and protein molecules can be tracked by neutron reflectivity incident from the substrate. Observing the assembly and disassembly of proteins under flow can help improve the performance of these devices.

Intrinsically disordered proteins (IDPs) are highly dynamic and do not have well-defined shapes. Depending on the interaction between IDPs and the surrounding material, e.g., lipid membranes, IDPs may quickly adopt stable conformations, complexes, and networks (Dyson and Wright, 2002). Time-resolved measurements can elucidate the mechanisms of protein assembly, adding to the understanding of the molecular basis of neurodegenerative and other diseases.

QIKR is designed to address the type of problems surveyed above. Its horizontal sample orientation and ability to perform measurements in the θ–θ scattering geometry (horizontal surfaces) enable study of lipid monolayers on water as well as lipids and other amphiphiles at liquid–liquid interfaces. The use of cinematic measurements and the unprecedented STS flux to resolve time dependence promise to open a new window onto membrane kinetics.

Fundamentals of neutron specular reflectometry

Neutron reflectometry exploits differences in the scattering properties of atoms to probe interfacial structure. Neutrons behave as waves, described by the Schrödinger equation and so, analogous to photons, reflect and refract at discontinuities in refractive index. The neutron refractive index depends on the scattering properties of a material's constituent atoms and how densely those atoms are packed in space (Squires, 2012; Klein and Werner, 1983),

$$n = \sqrt{1 - \frac{\lambda^2}{\pi}\frac{b}{V}} = \sqrt{1 - \frac{\lambda^2}{\pi}\frac{\rho N_A}{M}b} \approx 1 - \frac{\lambda^2}{2\pi}\frac{\rho N_A}{M}b, \qquad (1)$$

where λ is the neutron wavelength, ρ the mass density of the material through which the neutron wave passes, N_A Avogadro's number, M the molecular mass of a formula unit characteristic of the material (e.g., crystal unit cell or monomer stoichiometry), and b is the sum of neutron scattering lengths (the coherent scattering cross section is $4\pi b^2$) of the atoms within the formula unit. The quantity $\rho N_A/M$ defines the inverse of the volume V occupied by the formula-unit atoms. The b/V formulation is useful when treating mixtures, such as amphiphilic molecules spread on a water surface. Neutrons scatter from both the atom's nucleus and magnetically from unpaired valence electrons (Squires, 2012; Ankner and Felcher, 1999). Coherent spin-dependent scattering is not present for most atoms, so we omit consideration of it here for simplicity of presentation. The dependence of b on the neutron–nucleus interaction via the strong force means n is determined by isotopic (Sears, 1992) rather than atomic composition, a characteristic exploited to create contrast, most commonly by substituting deuterons (^{2}H) for protons (^{1}H), and also used in battery studies (^{6}Li and ^{7}Li) and other applications where relevant isotopes are available.

Neutron reflectometry comprises the measurement of the reflected intensity of a neutron beam directed onto a sample surface or more generally onto the interface between two refractive media. The reflection and refraction of neutrons from an interface obeys the same mathematics as that of photons i.e., Snell's Law (Born and Wolf, 1980), which is equivalent as well to the quantum-mechanical one-dimensional particle in a box (Cohen-Tannoudji *et al.*, 1977). In these treatments, a wave traveling through a refracting medium impinges on an interface with a medium of differing refractive index (Fig. 1). A portion of the incoming wave is specularly reflected at an exit angle equal to the incident angle, with the remainder being transmitted into the other medium. This elastic scattering process

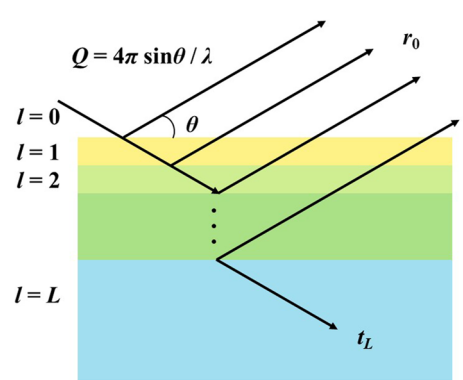

FIG. 1. A plane wave (wavelength λ) is incident from the left at an angle θ onto a film consisting of a sequence of L refracting slabs. The wavevector transfer Q is proportional to the momentum change of reflected relative to incident waves [Eq. (2)]. Waves specularly reflected from each successive interface combine coherently to produce a reflected wave of amplitude r_0 (Parratt, 1954). A transmitted wave of amplitude t_L upon reflection proceeds through a semi-infinite substrate medium.

is characterized by a change in momentum between reflected and incident waves,

$$\Delta p = \hbar Q = \hbar \frac{4\pi \sin \theta}{\lambda}, \tag{2}$$

where p is the component of the wave's momentum normal to the reflecting interface, $\hbar$ Planck's constant divided by 2π, θ the angle of incidence of the wave onto the interface, and λ its wavelength. The wavevector transfer Q, dependent on incident angle and wavelength, characterizes the specular reflectivity process. The scattering length density, Σ, related to the difference of a material's refractive index from 1 (of order 10^{-6} for neutrons), connects kinematic and refractive properties [Eqs. (1) and (2)],

$$\Sigma \equiv \frac{b}{V} = \frac{\rho N_A}{M} b = \frac{Q_c^2}{16\pi}, \tag{3}$$

where the critical wavevector Q_c is the wavevector below which a wave is totally reflected from the interface ($r_0 = 1$).

The wave-equation solution for the reflected amplitude r_0 may be extended to an arbitrary number of interfaces between incident and substrate media (Parratt, 1954). Essentially, one applies Snell's law in turn at each interface to account for the deflection of the transmitted waves,

$$Q_l = \sqrt{Q^2 - Q_{\mathrm{cl}}^2} = \sqrt{Q^2 - 16\pi\Sigma_l}, \tag{4}$$

where index l enumerates the sequence of refracting layers. Refractive gradients of arbitrary shape may be represented as sequences of layers of varying thickness and scattering length density (SLD) (Ankner and Majkrzak, 1992) and the interpretation of specular reflectivity data consists of fitting parametrized models of these refractive gradient distributions. The remainder of this work describes how QIKR will carry out the measurements depicted schematically in Fig. 1.

QIKR DESIGN

General requirements

The range of scientific fields served by QIKR is large, requiring specialized sample environments to interrogate solid and free liquid surfaces as well as solid/liquid, liquid/liquid, and solid/solid internal interfaces. Free liquid and liquid/liquid experiments (and to a lesser extent rheology) are constrained in that the sample surface is defined by gravity and so cannot be tilted. The incident reflection angle in these cases must be defined by deflecting (Campbell *et al.*, 2011) or sampling the angular divergence of the incident neutron beam (Ankner *et al.*, 2002). Free liquid surfaces and upper-subphase-transmitting liquid/liquid interfaces require a downward-directed incident beam, while lower-subphase-transmitting liquid/liquid interfaces need an upward-directed incident beam. Solid and solid/liquid samples can be tilted and generally are not constrained by the incident beam direction. However, delicate or massive sample environments, such as a rheometers, may also benefit from a non-tilted sample. Therefore, to address the interests of the entire scientific community, QIKR will offer both downward- and upward-directed incident beams.

Collecting data rapidly and accurately is important for all experiments and the neutron flux of the STS will enable experiments with unprecedented time resolution. True kinetic measurements must be collected at a single instrument setting covering the Q range of interest. The key parameter for such measurements is the dynamic range D accessible in a single instrument setting, which for a pulsed neutron source utilizing a single incident angle θ and time-of-flight to determine neutron wavelength may be written as

$$D \equiv \frac{Q_{\max}}{Q_{\min}} = \frac{\lambda_{\max}}{\lambda_{\min}} = 1 + \frac{h}{m}\frac{1}{L}\frac{1}{f}\frac{1}{\lambda_{\min}}, \tag{5}$$

where the ratio between the maximum and minimum wavevectors (or wavelengths) for a given measurement depends on Planck's constant h, the neutron mass m ($h/m = 3956.0$ m Hz Å), the neutron-source–detector distance L, the minimum wavelength $\lambda_{\min}$, and the source repetition frequency f. Since the neutron velocity $v = L/t$, for instruments employing neutron time-of-flight to determine wavelength, $D = v_{\max}/v_{\min} = t_{\max}/t_{\min}$ as well (recall $\hbar^2 k^2/2m = mv^2/2$ and $k = 2\pi/\lambda$). To determine neutron wavelength from time-of-flight, faster neutrons created by a succeeding pulse must not overrun slower neutrons created by the current pulse and so $t_{\max} = t_{\min} + f^{-1}$. Putting all this elementary physics together yields Eq. (5). On a time-of-flight instrument, large dynamic range is achieved by a short instrument on a low-frequency source utilizing short-wavelength neutrons. Accessing a dynamic range of 10 or more (e.g., $0.02 < Q < 0.2$ Å^{-1}) in a single instrument setting enables cinematic data collection for most samples.

The 15 Hz STS repetition rate allows a much larger wavelength bandwidth than is available at the 60 Hz Spallation Neutron Source (SNS) first target station (FTS), but to achieve true single-setting operation for most samples, QIKR must be able to run in pulse-skipping mode at 7.5 Hz, using only every other pulse from the accelerator. In addition, while optimizing transport of neutrons at peak moderator flux ($\lambda_{\min} = 2.5$ Å) is essential to maximize Q bandwidth and minimize counting time, the instrument will also be capable of operating at 15 Hz and in different wavelength bands. In such modes, one spans the full Q range with multiple incident beam angles.

The scientific interests of the QIKR user community require measurement of materials at solid and solid/liquid interfaces (θ–2θ geometry) as well as free liquid and liquid/liquid interfaces (θ–θ geometry). In addition, QIKR should be able to measure using beams incident from both above (e.g., free liquid) and below (e.g., liquid/liquid from the lower subphase) the sample interface (Fig. 2). In addition, there must be sufficient space available to mount and operate a variety of sample environments.

Wavevector resolution for specular reflectometry depends on wavelength (time-of-flight) and angular relative resolutions added in quadrature,

$$\frac{\delta Q}{Q} = \sqrt{\left(\frac{\delta\lambda}{\lambda}\right)^2 + \left(\frac{\delta\theta}{\theta}\right)^2}. \tag{6}$$

The coupled H_2 moderators planned for STS and the short flight path required to achieve a broad wavelength bandwidth imply a minimum relative Q resolution given by neutron emission time

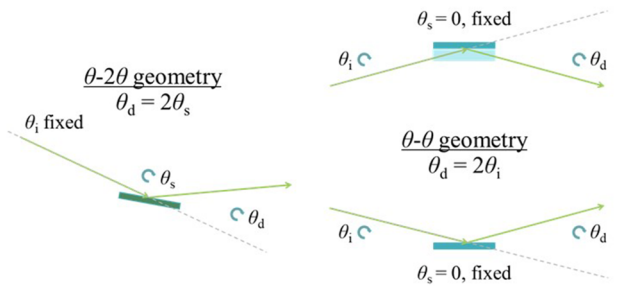

FIG. 2. Reflectometry scattering geometries. (left) θ–2θ geometry, in which incident angle θ_i is fixed and the sample and detector are rotated with specular condition at $\theta_d = 2\theta_s$. (right) θ–θ geometry where incident angle is varied or sampled, the sample incident angle is fixed, and $\theta_d = -\theta_i$ for specular reflectivity from upward-directed (top) and downward-directed (bottom) beams.

uncertainty $\delta t/t$ (hence, λ and Q) of about 0.02. While most experiments will be well served at that resolution, when measuring thin-film (e.g., lipid monolayer) kinetics, a user should be able to relax beam angular resolution and gain flux to improve time resolution. The considerations described above may be summarized in the following list of requirements:

- QIKR sample stage and environs must be spacious and equipped with utilities to accommodate a wide range of sample environment equipment.
- The QIKR instrument enclosure should be designed to minimize sample environment setup time and sample alignment time.
- QIKR must operate in both θ–2θ (solid and solid/liquid samples) and θ–θ (air/liquid and liquid/liquid samples) scattering geometries.
- QIKR must collect data using incident beams from both above and below the sample horizon.
- QIKR must be able to operate at 7.5 Hz (in addition to the 15 Hz source frequency) to maximize wavelength bandwidth.
- QIKR must transport all potential neutron phase space trajectories (space and divergence) of neutrons at the spectrum peak ($\lambda_{\min}$) for $0.02 < \delta\theta/\theta < 0.07$.
- QIKR should be placed as close to the moderator as possible to maximize wavelength bandwidth.

In addition to the more general requirements listed above, there are requirements common to most reflectivity measurements, such as beam footprint (sample size) and Q range. These parameters as well as resolution and dynamic range requirements discussed above are given in Table I.

Floor plan and physical dimensions

Considered as a whole, the requirements listed above prove difficult to satisfy on a single instrument. Geometry places limits on the working area available to an instrument that must have a short flight path amid converging neighboring beamlines. Achieving low background also becomes more challenging the closer one gets to the neutron source as does blocking the view of the neutron and gamma prompt flashes when the proton beam strikes the target. Providing a range of incident beam angles to achieve the required Q range using the available wavelengths in the θ–θ scattering geometry is likewise challenging. Accessing that range of incident angles from both above and below a gravity-defined sample horizon is harder still. These challenges along with the required flexibility in accommodating sample environments have led us to propose an instrument composed of two independently operable end stations (Fig. 3).

TABLE I. QIKR operating parameters.

Parameter	Value
Beam footprint at sample	Variable from 5 × 10 to 25 × 75 mm^2
Q range (θ–θ geometry)	$0.008 < Q < 0.35$ Å^{-1}
Q range (θ–2θ geometry)	$0.005 < Q < 0.50$ Å^{-1}
Q resolution	$0.02 < \delta Q/Q < 0.07$
Dynamic range D	10

The lower end station (QIKR-L), featuring a downward-directed beam, can perform free liquid measurements (e.g., Langmuir trough and upper-subphase-incident liquid/liquid). The upper end station (QIKR-U) is intended specifically for liquid/liquid reflectivity measurements with the lower subphase serving as the incident medium and rheometry in which shear is applied from above. Either station will be able to handle bulky, massive, or delicate sample environments that are best not tilted. The vertical angle of the incident beam is only determinative for experiments performed in the θ–θ scattering geometry, where the sample cannot be tilted. Both stations will be outfitted with sample and detector positioning systems to enable experiments in the θ–2θ scattering geometry as well.

To provide sufficient space in the independent end-station caves, QIKR-U will be longer than QIKR-L. The consequent reduction in dynamic range [Eq. (5)] is a sacrifice needed to satisfy space needs for both stations. The QIKR-U dynamic range (at 7.5 Hz) nonetheless equals or exceeds that of most existing instruments. Independent neutron optical systems will view the same coupled H_2 cylindrical moderator with a peak flux at 2.5 Å. Due to the intrinsic $\sim Q^{-4}$ decrease in reflectivity with Q, we have defined the smallest usable wavelength $\lambda_{\min}$ to be the spectral peak of the moderator—greatest flux at lowest reflectivity. Given the requirement that QIKR not encroach on adjacent instruments, the closest we could locate QIKR-L was at a moderator–detector distance of 20 m, with QIKR-U staggered back to 24 m. To access required Q ranges in the θ–θ geometry (see neutron guide design below),

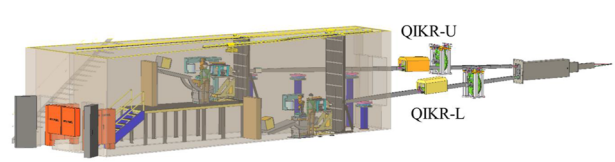

FIG. 3. Oblique side view of the QIKR lower (QIKR-L) and upper (QIKR-U) end stations and guide paths. The stations will be physically separated and operated independently.

TABLE II. Spatial, spectral, and timing characteristics of the lower (QIKR-L) and upper (QIKR-U) end stations and the beam angle relative to horizontal, γ_{guide}.

Station	L (m)	$\lambda_{\min}$ (Å)	f (Hz)	D	γ_{guide} (deg)
QIKR-L	20.0	2.5	15	6.3	−2.5
			7.5	11.5	
QIKR-U	24.0	2.5	15	5.4	2.5
			7.5	9.8	

the incident beams are inclined (γ_{guide}) 2.5° downward and upward for QIKR-L and QIKR-U, respectively. These parameters and the resulting dynamic ranges are shown in Table II.

Neutron transport (guide)

In addition to enhancing neutron brilliance transport, supermirror guides filter out high energy neutrons and provide angular divergence to access the full Q range required for θ–θ measurements (Table I). Figure 4 shows scaled vertical and horizontal schematics of the QIKR-L components. QIKR-U is essentially similar, differing only in vertical inclination, overall length, and chopper position. As with the FTS Liquids Reflectometer, QIKR utilizes multichannel benders rather than T_0 choppers to eliminate the prompt flash of fast neutrons from the target and moderator. In addition to the spatial impracticality of placing two T_0 choppers near the monolith (which could be solved by only building one end station), pulse-skipping operation at 7.5 Hz would be compromised. The T_0 chopper must block every pulse and so must run at 15 Hz, meaning it would transit the guide in the middle of the 7.5 Hz wavelength frame to block the unwanted pulse. To prevent the data acquisition issues associated with this transit, we have chosen to use a multichannel bender, which also allows extraction of two beams.

The other primary guide function is to supply angular divergence for measurements in the θ–θ geometry. The 3 × 3 cm^2 STS cylindrical moderator will be smaller and brighter than the 10 × 12 cm^2 FTS moderators. We image this small source using a long diverging ballistic guide section followed by a shorter converging taper in which the neutron population exiting the ballistic section is split into three: a central beam passing without reflection out the tapered exit and two satellite reflections from the bottom and top tapered surfaces that exit at shallower and steeper angles, respectively. The dimensions and coatings of the components of the QIKR-L and QIKR-U transport systems are given in Tables III and IV, respectively. The two guide systems are functionally identical, QIKR-U being 4 m longer with the chopper a meter farther back. The concept of phase space acceptance is useful in assessing neutron optical performance. The set of all possible trajectories through which a neutron can pass through a component defines the acceptance of that component. Components may be arrayed in series and acceptance passed from one component to the next (Carpenter and Mildner, 1982). The optical components used in QIKR are rectilinear, so there is no mixing of trajectories, and the acceptance may be written as the product of coordinate acceptances transverse to the beam propagation direction,

TABLE III. Components of QIKR-L guide and their lengths l, input distance from the neutron moderator L_{in}, width w, input h_{in}, height at output h_{out}, supermirror guide coating as a multiple m of the Q_c of nickel, and the number of channels in the component $n_{channels}$. The radius of curvature of the Ballistic Bender is 173 m.

Component	l (cm)	L_{in} (cm)	w (cm)	h_{in} (cm)	h_{out} (cm)	Coating (m)	$n_{channels}$
Source volume	200.0	0.0	3.0	3.00	2.65	···	1
Ballistic bender	622.0	200.0	3.0	2.65	6.76	5	3
Chopper gap	7.3	822.0	3.0	6.76	6.81	···	1
Ballistic guide	482.2	829.3	3.0	6.81	10.00	5	1
Tapered guide	287.5	1311.5	3.0	10.00	2.00	5	1

$$A(x, \gamma_x, y, \gamma_y, \lambda) = A_x(x, \gamma_x, \lambda) A_y(y, \gamma_y, \lambda), \tag{7}$$

where x and y are the transverse spatial coordinates and γ_x and γ_y the angles a given trajectory makes with respect to the component centerline. The function of optical components utilizing neutron reflection generally depends on neutron wavelength λ as well.

Using the acceptance framework (Ankner *et al.*, 2002), we can assess how well the QIKR guide system addresses our requirements. Since the QIKR-U is functionally equivalent to QIKR-L, we confine our discussion to QIKR-L. Integrating acceptance over both spatial and angular coordinates yields the total volume of phase space passed by the guide system. The integrated horizontal acceptance ($\int A_x dx d\gamma_x$) of the QIKR-L guide system (to the end of the Tapered

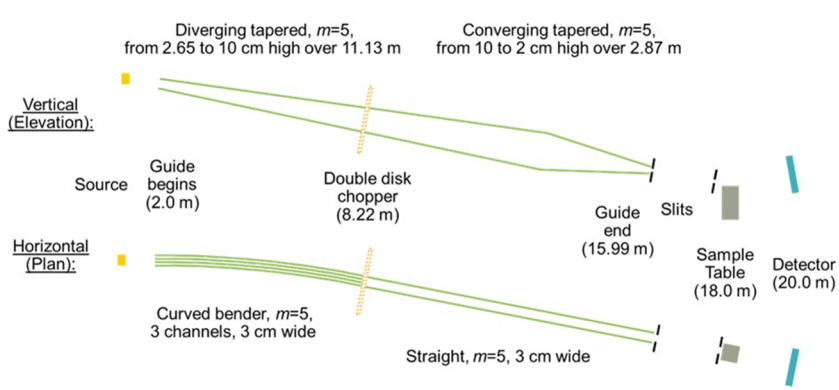

FIG. 4. Beamline schematic for the downward-directed QIKR-L beamline showing components and their distances from the neutron source (moderator).

TABLE IV. Components of QIKR-U guide and their lengths l, input distance from the neutron moderator L_{in}, width w, heights at input and output h_{in} and h_{out}, supermirror guide coating as a multiple m of the Q_c of nickel, and the number of channels in the component $n_{channels}$. The radius of curvature of the Ballistic Bender is 173 m.

Component	l (cm)	L_{in} (cm)	w (cm)	h_{in} (cm)	h_{out} (cm)	Coating (m)	$n_{channels}$
Source volume	200.0	0.0	3.0	3.00	2.65	···	1
Ballistic bender	622.0	200.0	3.0	2.65	5.68	5	3
Ballistic guide	103.7	822.0	3.0	5.68	6.18	5	1
Chopper gap	7.3	925.7	3.0	6.18	6.21	···	1
Ballistic guide	778.5	933.0	3.0	6.21	10.00	5	1
Tapered guide	287.5	1711.5	3.0	10.00	2.00	5	1

Guide) is plotted along with the acceptance of the same guide system straightened out with no blades in the Ballistic Bender (Fig. 5). The bender system delivers on the twin requirements of transporting the peak spectral flux (acceptance transmission >0.98 for $\boldsymbol{\lambda} > 2.5$ Å) and eliminating fast neutrons (a hard cutoff for $\boldsymbol{\lambda} < 0.17$ Å due to the segmentally curved Ballistic Bender). The Tapered Guide (TG) provides angular divergence for $\boldsymbol{\theta}$–$\boldsymbol{\theta}$ measurements and its performance may be evaluated by integrating the vertical acceptance over the spatial coordinate ($\int A_y dy$) to simulate a rocking curve. Figure 6 plots the spatially integrated vertical acceptance against the angular deviation of the neutron trajectory relative to the TG centerline. Three beams are produced: along the centerline and at ±1.67° relative to it (±1.63° for QIKR-U). Apertures downstream of the TG exit (see Fig. 4) are used to direct a beam at the chosen incident angle onto an interface in the $\boldsymbol{\theta}$–$\boldsymbol{\theta}$ scattering geometry. Table V shows the resulting single-measurement Q ranges for 15 and 7.5 Hz. These individual-angle ranges provide sufficient overlap for non-cinematic coverage of the full Q range at both 15 and 7.5 Hz as well as a wide enough range to enable cinematic measurements in most cases, particularly for the $\boldsymbol{\gamma}_{guide} = \pm 2.5°$ centerline beams. Gravity will affect where the longest-wavelength neutrons strike the diverging and converging guide sections and may alter the spectra of the satellite beams shown in Fig. 6, an effect we will assess via Monte Carlo simulation.

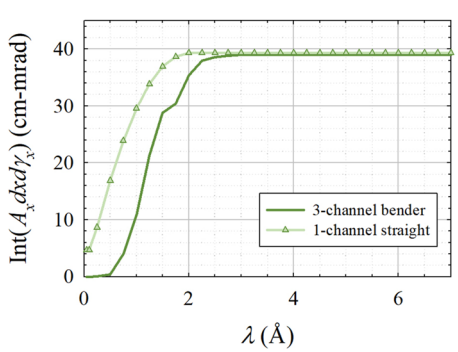

FIG. 5. Horizontal QIKR-L acceptance integrated over space and angle plotted vs wavelength λ. The bender filters out fast neutrons and transmits >0.98 of the integrated acceptance for $\lambda > 2.5$ Å.

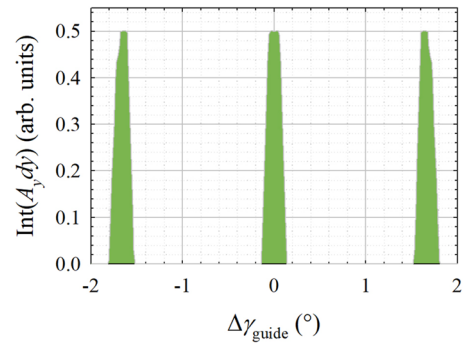

FIG. 6. Vertical QIKR-L acceptance integrated over the spatial coordinate plotted against the deviation of the trajectory from the centerline of the Tapered Guide. Beams are present along the centerline and at ±1.67° relative to it. The 2.5° downward tilt of QIKR-L yields incident beams at 0.83°, 2.5°, and 4.17°.

Operationally, we expect the spectra to vary between the different satellites and will normalize the data accordingly.

Wavelength bandwidth control

Definition of wavelength bandwidth at both the 15 Hz source frequency and for pulse-skipping at 7.5 Hz will be done using a single counter-rotating double-disk bandwidth chopper and a frame-overlap mirror (FOM) on both the QIKR-L and QIKR-U beamlines. Controlling bandwidth on a low-repetition-rate source such as the STS is easier than on the 60 Hz FTS simply because there are fewer pulse trains to sort through in the guide. One double-disk chopper and a frame-overlap mirror (FOM) suffice (Fig. 7). One sets the phase of a rotating chopper so that the peak intensity of the center wavelength in the selected band passes the chopper at the dead-center angle of its open window. After rotating through 2π, the chopper opens again. At each cyclic chopper opening, neutrons from past pulses are let through, in addition to those desired from the current pulse. The FOM is set at such an angle that it reflects away

TABLE V. Accessible Q ranges for measurements in θ–θ geometry for the three beams produced by the QIKR-L and QIKR-U guide systems as a function of source frequency f, dynamic range D [for $\lambda_{\min} = 2.5$ Å, see Eq. (5)], and beam angle of incidence θ.

Station	f (Hz)	D	θ (deg)	$Q_{\min}$ (Å^{-1})	$Q_{\max}$ (Å^{-1})
QIKR-L	15	6.3	−0.83	0.012	0.073
			−2.50	0.035	0.219
			−4.17	0.058	0.366
	7.5	11.5	−0.83	0.006	0.073
			−2.50	0.019	0.219
			−4.17	0.032	0.366
QIKR-U	15	5.4	0.87	0.014	0.076
			2.50	0.041	0.219
			4.13	0.068	0.362
	7.5	9.8	0.87	0.008	0.076
			2.50	0.022	0.219
			4.13	0.038	0.362

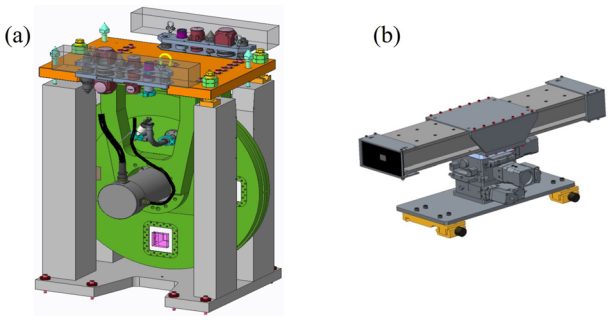

FIG. 7. Renderings of (a) STS standard double-disk chopper and (b) frame-overlap mirror (FOM).

these unwanted longer wavelength neutrons. In Fig. 8, the chopper has been phased to admit $2.5 < \lambda < 14.4$ Å and an $m = 3$ supermirror coated FOM array set at 8.2° to reflect away $\lambda > 28$ Å neutrons for the most divergent beams envisioned. The imperfect reflectance of supermirrors above the nickel critical angle has been mitigated in the existing Liquids Reflectometer by stacking three front- and back-coated mirrors in the beam, which reduces the 0.1 unwanted transmission of a single mirror surface at the worst-angle to 10^{-6} (six mirror surfaces). We will confirm the adequacy of this performance and evaluate other filtering options (Saerbeck *et al.*, 2018) via Monte Carlo simulation.

Precise alignment and sharp wavelength rejection of the FOM are crucial to pulse-skipping operation at 7.5 Hz. In addition to rejecting neutrons from previous desired pulses, the system must also completely reject neutrons from the pulse immediately preceding the desired one and allow through twice the bandwidth as at 15 Hz. Figure 9 depicts this trickier situation. The desired wavelength band lies close to that of neutrons passed by the chopper from the rejected pulse (neutrons from earlier desired pulses are present only for $\lambda > 45$ Å). The chopper disk edge must transit the beam sufficiently rapidly that both desired and rejected wavelength bands have a sharp cutoff and the FOM must cleanly reject neutrons within a narrow wavelength gap.

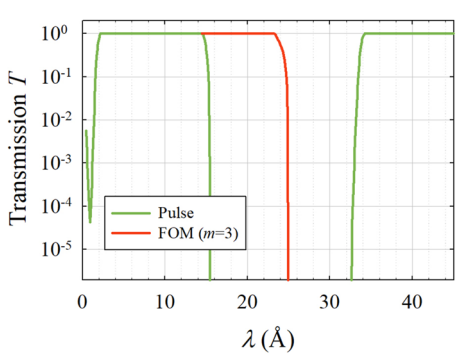

FIG. 8. Transmission functions of QIKR-L chopper rotating at 15 Hz phased to deliver $2.5 < \lambda < 14.4$ Å (green) and an $m = 3$ frame-overlap mirror (FOM) inclined at 8.2° to the beam (red).

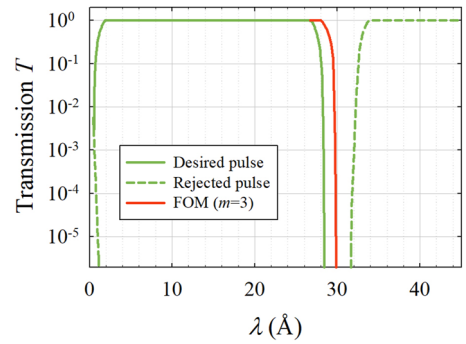

FIG. 9. Transmission functions of QIKR-L chopper rotating at 7.5 Hz phased to deliver $2.5 < \lambda < 26.2$ Å (green) and an $m = 3$ frame-overlap mirror (FOM) inclined at 8.6° to the beam (red). The chopper and FOM must also reject the previous pulse (dashed green).

The double-disk chopper plays a crucial role implementing pulse-skipping and thereby enabling routine cinematic operation at QIKR. Due to the intrinsic uncertainty of neutron emission times from the moderator, short-wavelength neutrons emitted late can arrive at the chopper and find it open. If this leakage bleeds into the long-wavelength edge of the stroboscopically collected pulses, assignment of wavelength to time-of-flight will fail. In Figs. 8 and 9, we have assumed we can use 90% of the calculated frame bandwidth to extract the stated wavelength ranges. The angular opening of a single-disk chopper is cut by the manufacturer and can only be changed by swapping out the disk. The angular opening of a counter-rotating double-disk chopper depends on the relative phases of the two disks and so can be optimized to yield the largest practical wavelength bandwidth. Additionally, the twice-faster transit time of the counter-rotating disks enables mounting the QIKR-L chopper to the side of the guide and closer to the moderator without encroaching on the neighboring instrument. Table VI lists the parameters of the wavelength band defining components.

Incident beam definition, sample and detector positioning

Reflectometry requires precise beam definition and sample positioning. To enable experiments on free liquid and liquid/liquid samples in the θ–θ geometry, both QIKR-L and QIKR-U will be horizontal-surface instruments. In Fig. 10, upstream and downstream apertures s_u and s_d define a beam incident at an angle θ onto a sample within a footprint F determined by the apertures and the distance between them (l_{ud}), which in addition determine the angular divergence of the incident beam $\delta\theta$.

Generally, one wishes to confine a beam of given angular resolution within a limited footprint (e.g., to avoid illuminating gaskets or mounting hardware and to improve normalization accuracy). Turning the problem around and performing a bit of algebra (see the complete version in the Appendix), we can use these constraints to define the slit apertures in terms of the desired footprint F and relative resolution $\delta\theta/\theta$ using the small-angle approximation $\sin\theta \approx \theta$,

$$s_u \approx l_{ud}\theta(\delta\theta/\theta), \tag{8}$$

TABLE VI. Parameters of the QIKR bandwidth defining components: type of chopper, distance from the neutron source L, width of beam cut (tangential to chopper-disk rotation) w, height of beam cut (radial) h, absorption of chopper blades for 1 Å neutrons, and guide coating on the frame-overlap mirror (FOM) as a multiple m of the nickel Q_c.

Station	Chopper	L (m)	w (cm)	h (cm)	Absorption (Å^{-1})	FOM (m)
QIKR-L	Counter-rotating double disk	8.2	6.8	3.0	10^{-5}	3
QIKR-U	Counter-rotating double disk	9.3	3.0	6.2	10^{-5}	3

$$s_d \approx \frac{l_{ud}\theta[F - l_{ds}(\delta\theta/\theta)]}{l_{ud} + l_{ds}}, \tag{9}$$

where the dimensions are defined in Fig. 10. The preceding derivation is a basic application of phase space acceptance. The integrated acceptance (again using the small-angle approximation) is just the product of the downstream aperture and twice the steepest angle (relative to the centerline) through the slits,

$$\int A_y dy d\gamma_y \approx \frac{s_u s_d}{l_{ud}}. \tag{10}$$

The function of the instrument downstream of the guide is to direct a precisely defined beam onto a precisely oriented sample and collect the reflected neutrons in a precisely positioned detector. While there are many motors in a reflectometer, there are only a handful of essential angular and linear parameters. In addition to the apertures defined in Eqs. (8) and (9), the inclination angles of the incident beam (γ_i), the sample (γ_s), and the detector (γ_d) relative to horizontal are essential (Fig. 11). The angle of the beam onto the sample is given by (recall Fig. 2)

$$\theta_i = \gamma_s - \gamma_i \equiv \theta. \tag{11}$$

Likewise, the detector angle is

$$\theta_d = \gamma_d - \gamma_i. \tag{12}$$

In Fig. 11 and the preceding equations, downward-directed angles are negative and upward-directed angles positive. These expressions hold for both θ–θ and θ–2θ scattering geometries (Fig. 1). Accurately and precisely defining the upstream and downstream beam apertures and the angles of the incident beam, sample, and reflected beam is essential for specifying Q and controlling the resolution and footprint on the sample.

Positioning the incident optics, sample, and detector will be carried out in a similar fashion as is done currently on the FTS Liquids Reflectometer (Fig. 12). An incident table will support the upstream and downstream slits (s_u and s_d) and their inclination angle γ_i. The downstream slit will be mounted on an extensible arm allowing placement as close as possible to the sample (minimize l_{ds}—see Fig. 10) for a given sample environment to maximize the incident intensity within a specified beam footprint. A Sample Table will position the sample translationally and rotationally (including γ_s) and be sufficiently robust to support the burliest sample environments (e.g., vacuum chambers). We are currently assessing the relative merits of different positioning options, such as a goniometer stack vs a hexapod. The detector will be mounted on a detector arm able to rotate about axes transverse to the incident neutron beam in the plane of (γ_d) and normal to the sample surface. To allow more working space and room for sample environments, we are working to make the QIKR components more compact without sacrificing strength or stability (Fig. 13).

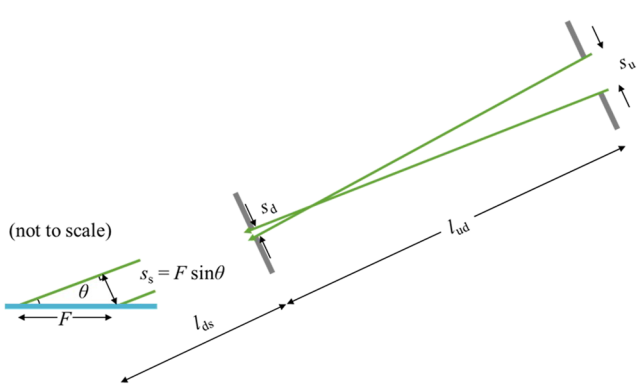

FIG. 10. Collimation geometry for reflectometry. The neutron beam (green) is collimated by upstream and downstream slits, s_u and s_d, a distance l_{ud} apart, passing onto a sample a distance l_{ds} from the downstream slit. The beam strikes the sample at an angle θ (generally <5°). Specifying a given footprint F and angular resolution $\delta\theta/\theta$ determines the slit values (see text).

Beam detection and data acquisition

Detectors at STS will need to handle increased count rates over broader wavelength bands than at FTS. The number of neutrons incident on the sample can be calculated if one knows the brightness of the moderator, which may be estimated using Monte Carlo methods (MCNPX) (Gallmeier *et al.*, 2016) and broadly follows the blackbody emission of an object at the temperature of the moderator. Figure 14 shows brightness as a function of neutron wavelength for the proposed 3 cm-diameter cylindrical coupled 20 K H_2 moderator at STS illuminated by 700 kW of proton power deposited

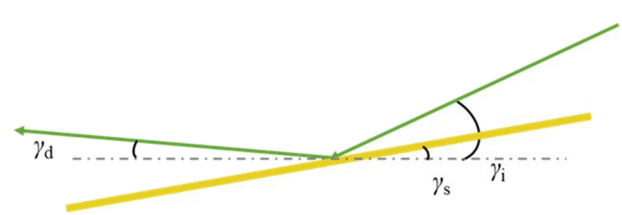

FIG. 11. In addition to upstream and downstream apertures s_u and s_d, the tilt angles of the incident beam (γ_i), sample (γ_s), and the reflected beam (γ_d) are essential parameters for defining the scattering wavevector Q.

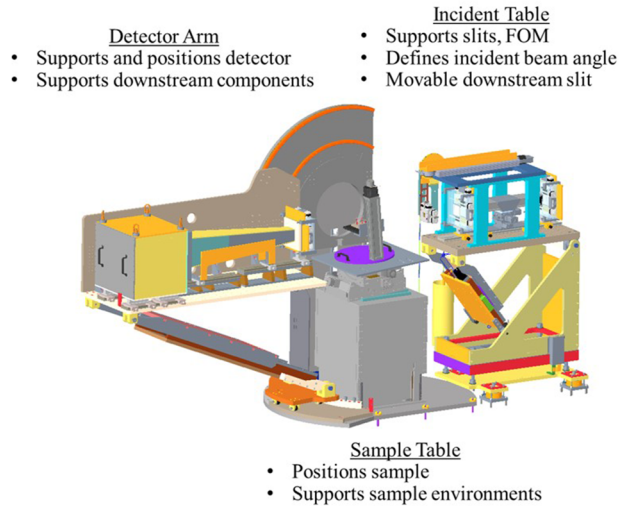

FIG. 12. First Target Station Liquids Reflectometer (FTS-LR) components downstream of the guide exit. QIKR will employ a similar arrangement.

on target at 15 Hz. Such a plot assumes moderator emission to be isotropic in angle and position on the moderator surface. This approximation is broadly valid in practice since the instruments are constructed nearly "face-on" with moderators and divergence angles are small. Under these assumptions, neutron intensity on sample may be written (Zhao *et al.*, 2013) as follows:

$$I(\lambda) = \Phi_b(\lambda) \int A(x, y, \gamma_x, \gamma_y, \lambda) dx dy d\gamma_x d\gamma_y, \tag{13}$$

where λ is the neutron wavelength, Φ_b is the source brightness, x, y and γ_x, γ_y are the position and angular divergence coordinates, respectively, of a neutron incident on the sample. The acceptance

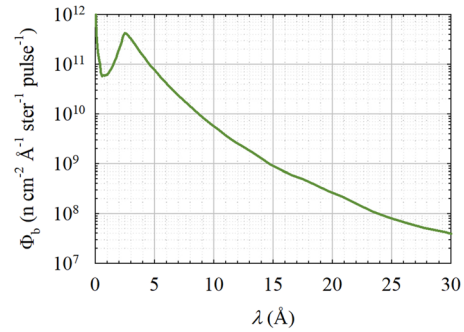

FIG. 14. Calculated brightness of STS cylinder moderator (Gallmeier *et al.*, 2016).

function A comprises the coordinates of neutrons emitted by the moderator capable of striking the sample [recall Eq. (7) and see the Appendix].

What count rates do we expect the QIKR-L guide system to deliver from the STS cylinder moderator to the sample? The settings in Table I span a wide range of operational conditions, from a tightly collimated beam onto a small sample to a relaxed collimation beam illuminating a large patch on a free liquid surface. Table VII shows two extreme settings: small, tightly collimated at the shallowest θ–θ angle ($\gamma_i = \theta = -0.83°$) and large with relaxed collimation at the steepest ($\gamma_i = -4.17°$). A more typical setting is also given for the central angle ($\gamma_I = -2.5°$). The most intense expected incident beam occurs for the steepest incident angle and the most wide-open collimation illuminating the largest footprint (the $I = -4.17°$ setting). Acceptance is independent of wavelength for $\lambda > 2.5$ Å (Fig. 5), so the space and angle integrals over horizontal and vertical coordinates in Eq. (10) operate as multiplicative factors on the brightness.

The result of these integrations, the wavelength-dependent count rate for the most intense beam is shown in Fig. 15. The 15 and

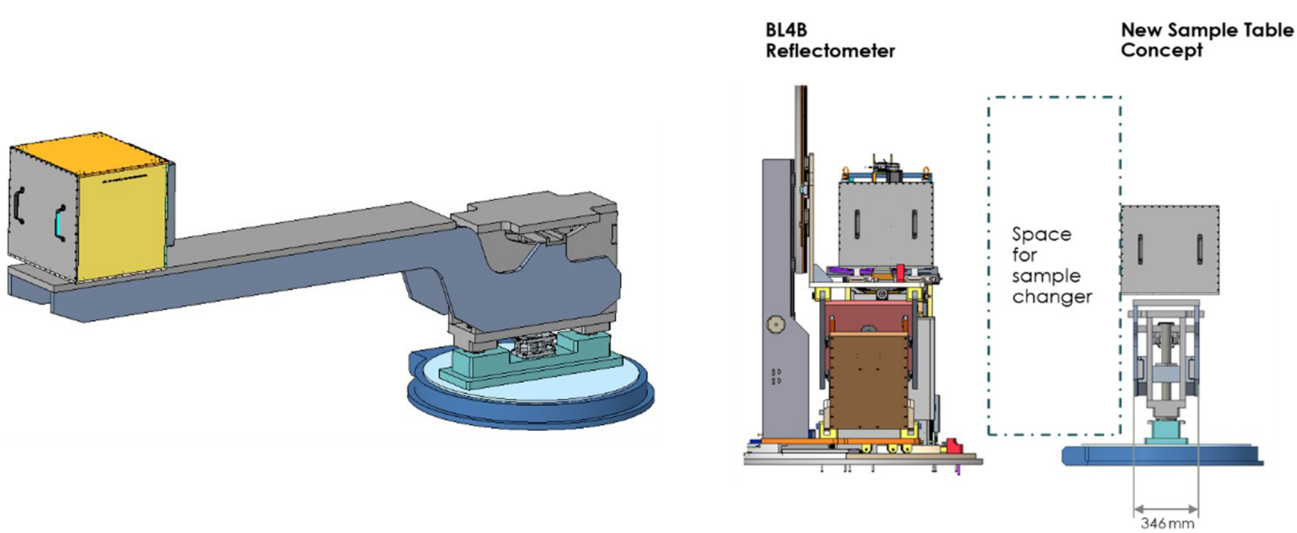

FIG. 13. Ongoing design effort on QIKR detector arm aimed at creating space without sacrificing stiffness or accuracy. Similar efforts are under way for the incident table.

TABLE VII. Settings for beam on sample at QIKR-L in θ–θ geometry in terms of incident angle γl_i (= θ here), relative beam divergence $\delta\theta/\theta$, beam footprint on the sample F, and horizontal beam aperture (in x) s_w. The upstream and downstream vertical apertures (in y) to illuminate F for l_{ud} = 190 cm and l_{ds} = 10 cm are s_u and s_d, respectively. The final two columns show the integrated horizontal and vertical acceptances.

γ_i (deg)	$\delta\theta/\theta$	F (mm)	s_w (mm)	s_u (mm)	s_d (mm)	$\int A_x dx dy_x$ (cm mradian)	$\int A_y dy dy_y$ (cm mradian)
−0.83	0.020	10	5	0.55	0.11	4.2	0.003
−2.50	0.025	30	25	2.07	0.31	24.1	0.124
−4.17	0.070	75	25	9.18	4.70	24.1	1.480

7.5 Hz transmission functions from Figs. 8 and 9, respectively, have been applied to Φ_b as well as a transmission function constructed from the curved-guide plot in Fig. 5. The peak count rate at 2.5 Å in a 0.14 Å-wide bin at 15 Hz is 1.6×10^7 ns^{-1}. Pulse-skipping at 7.5 Hz costs half the intensity but doubles the bandwidth.

The challenge for measuring reflectivity on QIKR will lie not only in the raw peak intensity, but rather in the broad wavelength bandwidth and consequent wide range of intensity. At 7.5 Hz, intensity on sample varies over nearly four orders in magnitude. To comprehend this challenge, consider how specular reflectivity is conventionally measured,

$$R(\lambda) = \frac{I_R(\lambda)}{I_D(\lambda)}, \tag{14}$$

where R is the absolute reflectivity, I_R the intensity reflected from the sample, and I_D the intensity of the direct beam onto the sample. In principle, this is simple. Measure the direct beam, measure the reflected beam, divide reflected by direct, and convert to $R(Q)$ via $Q = 4\pi \sin\theta/\lambda$. In practice, detectors have difficulty handling the instantaneous count rate for the direct beam, so one either attenuates the incident beam or samples a portion of it, e.g., with tighter slits. With the comparatively narrow wavelength bandwidths at the FTS (e.g., 3.4 Å for FTS-LR at 60 Hz), these approaches work well. Due to the wide range of intensity over the broader QIKR wavelength band (greater than 100 at 15 Hz and almost 10 000 at 7.5 Hz), reducing the intensity uniformly at all wavelengths (or worse) overcounts the short wavelengths. Using such normalization data would inject this statistical bias into every reflectivity dataset.

The dependence of reflectivity on wavelength offers a solution to this counting statistics problem and in addition can relieve the peak count rate burden on the detector. Neutron reflectivity from the smooth surface of a monolithic material such as quartz or water decreases as Q^{-4} at large Q, meaning it increases as λ^4. This dependence neatly counteracts the falloff in moderator brightness with wavelength. The direct beam in Fig. 16 is produced by the "conventional" settings in Table VII ($I_i = -2.5°$) at 7.5 Hz incident onto a D_2O surface. The chopper-selected ($2.5 < \lambda < 26.2$ Å) wavelength band produces reflectivity over $0.019 < Q < 0.22$ Å^{-1}. The constancy of the wavelength-dependent count rate (solid blue) over the entire wavelength range suggests an alternative, indirect way to measure the direct-beam intensity,

$$I_D(\lambda) = \frac{I_R(\lambda)}{R_{known}(\lambda)}. \tag{15}$$

If one knows the reflectivity of a standard reference sample, then the illuminating direct-beam intensity can be determined by dividing the measured reflected intensity by the known reflectivity curve. The indirectly measured direct-beam intensity I_D may then be used to normalize samples in the conventional fashion [Eq. (14)]. The reflectivity of pure materials without surface contamination, such as quartz and D_2O, is known with a high degree of confidence and $I_D(\lambda)$ measured over the full range of high-quality reference sample reflectivity data at a given θ. The falloff in reflected intensity at the shortest wavelengths (<5 Å) in Fig. 16, though, hints at the limitations and challenges of the indirect procedure. For a given incident angle and slit settings, one must be able to measure reference sample reflectivity out to the highest Q accessed by

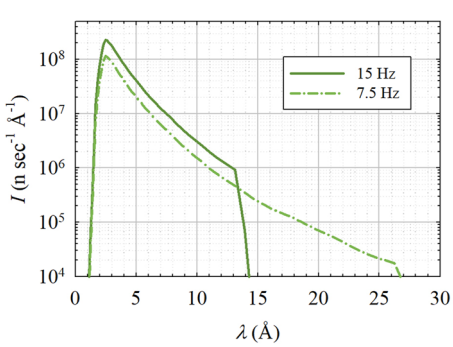

FIG. 15. Wavelength-dependent neutron current for the most intense expected beam on sample ($\gamma_i = -4.17°$ in Table VII) corrected for guide and chopper transmission.

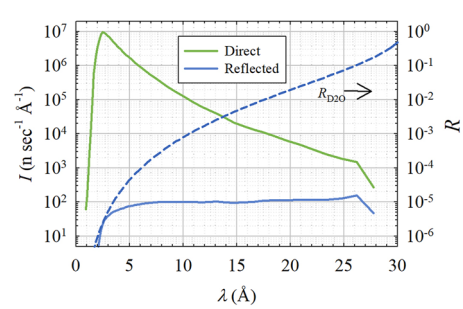

FIG. 16. Wavelength-dependent count rate for the direct beam incident at $\gamma_i = -2.5°$ (settings in Table VII – green) vs that of the beam reflected from D_2O (blue). D_2O reflectivity is shown in the blue dashed line with scale on the right.

the chosen wavelength band. For D_2O, incoherent scattering from the subphase limits one's ability to measure R to much below 10^{-6}, which is about 0.22 $Å^{-1}$ in Q at $\theta = 2.5°$. Quartz performs rather better, allowing R_{known} to be measured out to 0.3 $Å^{-1}$. Both these reference layers are currently in use at the FTS-LR (Phan *et al.*, 2020; Blair *et al.*, 2022) for normalizing pulse-skipping measurements at 30 Hz. Investigation of bootstrapping more complicated reference films featuring higher reflectivity at high Q (e.g., thin oxide layers on silicon substrates) is ongoing. If extending the maximum Q of the reference sample reflectivity proves infeasible, we may employ more conventional attenuated direct-beam measurements of overlapping low- and high-λ bands and splice them together, accepting the variation in statistical quality over the hybrid band. Implications for detector count rate of the indirect normalization procedure are clear from Fig. 16: a reduction in peak instantaneous count rate of 10^5. In the worst case, measuring at $I = -4.17°$ with the most relaxed resolution, the reflected intensity is of order several thousand counts per second and should be readily measurable using existing detector technology. In terms of spatial requirements, the smallest, most finely collimated beams envisioned ($\gamma_i = -0.83°$ in Table VII) produce beams at the detector no smaller than 1 mm high, while the coarse beam ($\gamma_i = -4.17°$) is not larger than 10 mm high. Collimated to 25 mm horizontally, beams will spread to 70 mm at the detector. Therefore, for specular reflectivity measurements, all the action takes place in a relatively confined rectangular area of 10×2 cm^2 and could be accommodated by a detector with relaxed horizontal resolution and a rectangular footprint. Off-specular reflectivity, though, demands a taller window. The 20×20 cm^2 view of the current FTS-LR detector has proven sufficient. The more restricted footprint of the specular beam may aid in construction (tiling) for some of the detector technologies under consideration. Use of a large-area position-sensitive detector enables correction of the gravitational deflection of the longest-wavelength neutrons after reflection from the sample by redefinition of the specular pixels over the wavelength band.

PERFORMANCE ESTIMATES

Brilliance transfer

The performance of an instrument depends crucially on how efficiently neutrons are transported from source to sample. Operating the instrument at relaxed resolution is one of the parameters specified in Table I. If one does not need angular resolution for a given measurement, can one exchange resolution for intensity? The small (3×3 cm^2) bright STS cylinder moderator favors higher resolution and smaller samples, broadly. Conversely, loosely collimated beams illuminating large samples (or sample footprints) are not so readily extracted. The derivation of collimating slit acceptance in the Appendix assumes sufficient phase space acceptance is delivered to the upstream slit that its divergence is determined solely by the slits. The filled parallelogram of Fig. 21 and trapezoidal rocking curve in Fig. 23 are characteristic of fully illuminated optics. Since most of the experiments run currently on the FTS-LR utilize $\delta\theta/\theta = 0.025$, the guide system was optimized to deliver full intensity at small angular divergence. Only users studying very thin films such as lipid monolayers can afford to significantly relax resolution. The results of this optimization are seen in Fig. 17, which plots vertical slit acceptance rocking curves on QIKR-L for a series of

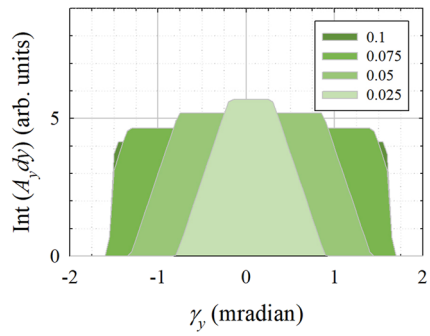

FIG. 17. Vertical coordinate acceptance rocking curves for the QIKR-L central beam in θ–θ geometry (Fig. 6, $\gamma_i = -2.5°$) with slits illuminating an $F = 30$ mm footprint (Table VII) for relative resolutions in the range of $0.025 < \delta\theta/\theta < 0.10$ ($l_{ud} = 190$ cm, $l_{ds} = 10$ cm).

relative angular resolutions ranging from 0.025 to 0.10 for the central beam ($\gamma_i = -2.5°$) illuminating a 30 mm footprint in θ–θ geometry. Both 0.025 and 0.05 are fully illuminated, with all needed trajectories illuminated. The 0.075 setting exhibits an absence of available phase volume in the truncated wings of the rocking-curve trapezoid. Attempting to extract $\delta\theta/\theta = 0.10$ results in a nonintuitive loss of integrated acceptance due to the reduction of downstream slit aperture s_d required to maintain the beam footprint (see Fig. 24). Trading resolution for intensity is only profitable out to $\delta\theta/\theta = 0.07$, as specified in Table I.

We have not yet considered the cost of guide imperfection. Unfortunately, neutron supermirrors are not perfectly reflective out to their nominal m value (multiple of the Ni critical reflection angle). Reflectivity is close to 1 up to the Ni critical angle, then declines linearly with angle out to the m value. For the $m = 5$ guides used here, reflectivity declines to about 0.75 at the nominal supermirror critical angle (SwissNeutronics, 2022). To estimate the cost of imperfect reflection, weigh the perfect-guide acceptance by 0.9 raised to the average number of bounces a neutron makes (tracked in the acceptance calculation). Consider the integrated acceptances plotted in Fig. 5. The reference uncurved straight guide with a direct moderator view features an integrated horizontal acceptance of 39.3 cm mradian, but each neutron bounces an average of 2.9 times off the guide walls, reducing the actual intensity delivered by a factor of $0.9^{2.9} = 0.74$. Imperfect reflection costs about a quarter of the neutrons in the baseline direct-view guide. The neutrons transiting the three-channel curved guide with an acceptance of 39.0 cm mradian bounce an average of 6.2 times, primarily due to the narrow channels costing $0.9^{6.2} = 0.52$ of what perfect guides would deliver. Since we do not live in a world of perfect guides, the correct factor to apply as the neutronic cost of the multichannel bender is $(0.52/0.74) \times (39.0/39.3) = 0.7$. The cost of the bender vs a direct moderator view and T_0 chopper is therefore about 30% of the intensity. In return, we do not have to deal with the chopper slug transiting the pulse-skipping wavelength band mid-frame and we have space to construct two end stations.

Simulated sample

The guide and chopper parameters and performance were calculated analytically as described above to optimize the design and

the resulting instrument was implemented for Monte Carlo simulation using McStas (Willendrup and Lefmann, 2020; Willendrup and Lefmann, 2021). A McStas virtual source was created at the exit of the guide and sampled by slits and a specularly reflecting sample using MCViNE (Lin *et al.*, 2019). The reflected beam passed onto a 2D position-sensitive detector, from which were generated NeXus event data files, then reduced like actual data (Shipman *et al.*, 2014).

The virtual source illuminated an Ir calibration film under several different experimental conditions. These measurements are shown in Fig. 18. The upper two curves (blue and red) are collected conventionally, using 1° and 4° incident angles at 7.5 Hz to span $0.009 < Q < 0.35$ Å^{-1}. For both measurements, the 1° data were collected in a single pulse; the 4° sets were collected for 10 min (blue) and 1 min (red). The third set was collected using a single incident angle of 2.5° for one minute. The base model for the Ir film was taken from a fit to data from an actual film measured on the FTS-LR. Despite being a noble metal, the Ir sputter deposited on a Si substrate exhibits a surface oxide layer as well as retaining an essentially intact native Si oxide layer at the substrate interface. Table VIII shows fits to reflectivity data with counting statistics generated from a McStas virtual source using slit settings that illuminate the sample in a 2 × 3 cm^2 footprint on a 5 cm-diameter substrate using a constant relative angular resolution $\delta\theta/\theta = 0.023$.

Each reflecting layer features a thickness d, a scattering length density Σ, and an rms interfacial width σ with the overlying layer. The two-setting 10-minute duration dataset (top, blue in Fig. 17) corresponds closely in quality to data we collect currently on the FTS-LR in about 80 min, validating our estimated QIKR intensity gain. Reducing the counting time of the higher angle to 1 min results in a notable decrease in fit quality, particularly for the interfacial widths. Interestingly, the single-setting 1 min dataset model is intermediate in quality and superior in that it does not require a 60–90 s instrument adjustment between settings. The poorer fit to the two-angle, one minute data shows how fit quality can vary subtly depending on choice of Q range and counting time. For the single-setting measurement, QIKR can simply be turned on, collecting data as the sample evolves under environmental stimuli. What portion of the time stream is of value and what time resolution is required may be sorted out post-experiment (Blair *et al.*, 2022). In general, determining interfacial widths of thin layers requires data acquisition to large Q and relatively long counting times. Finally, Fig. 17 and Table VIII show that a single selected Q range measurement can produce an excellent fit, particularly when interfacial width is not a critical parameter. In such cases, it will be possible to push data collection time below one minute.

TABLE VIII. Fitted model parameters for the datasets shown in Fig. 18, with the left column corresponding with the top blue dataset, the middle column to the middle red dataset, and the right column to the bottom green dataset. Thickness (d), scattering length density (Σ), and rms interfacial width (σ) were fitted for the Ir film, oxide layers above and below, and the Si substrate.

Parameter	Two angles (10 min)	Two angles (1 min)	One angle (1 min)
d_{IrOx} (Å)	39.8 ± 0.3	37.2 ± 1.5	39.6 ± 0.5
Σ_{IrOx} (10^{-6} Å^{-2})	2.57 ± 0.06	2.3 ± 0.3	2.60 ± 0.10
σ_{IrOx} (Å)	2.5 ± 0.6	1.6 ± 1.7	1.2 ± 1.0
d_{Ir} (Å)	459.1 ± 0.3	460.5 ± 1.2	461.6 ± 0.8
Σ_{Ir} (10^{-6} Å^{-2})	6.97 ± 0.02	7.04 ± 0.03	7.00 ± 0.03
σ_{Ir} (Å)	1.2 ± 0.3	7.3 ± 2.1	3.0 ± 0.8
d_{SiOx} (Å)	23.2 ± 0.6	28.6 ± 7.2	27.0 ± 5.0
Σ_{SiOx} (10^{-6} Å^{-2})	3.37 ± 0.08	3.3 ± 0.4	2.9 ± 0.4
σ_{SiOx} (Å)	1.1 ± 0.4	1.1 ± 2.2	4.6 ± 1.4
σ_{Si} (Å)	3.0 ± 1.1	8.2 ± 6.3	1.2 ± 4.4

SUMMARY

Cinematic data collection is not a new idea. The concept has been the paradigm for time-of-flight reflectometers since their inception (Sun *et al.*, 1989; Felcher *et al.*, 1987; and Felici *et al.*, 1988). In practice, as discussed above, the instrument must conform to the source and the space available for it, constraints that can be

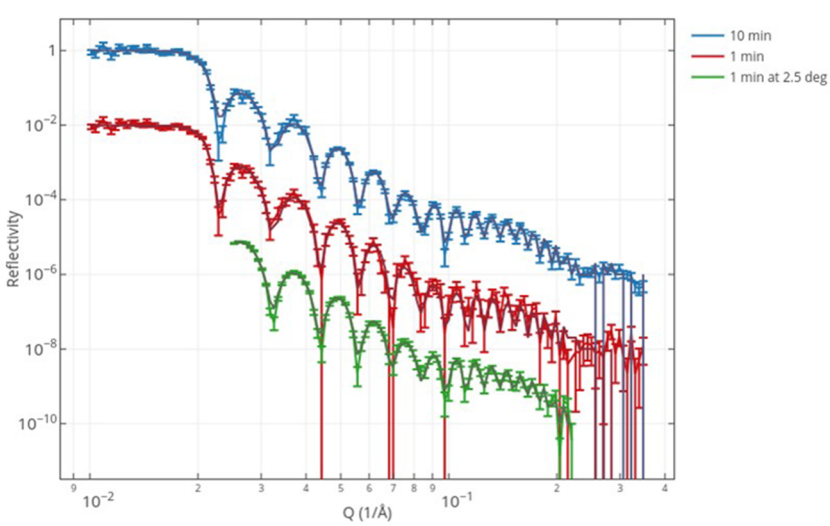

FIG. 18. Simulated 7.5 Hz STS-QIKR-L reflectivity from an Ir calibration film collected under three different conditions: (top, blue) measurements at incident angles $\theta = 1°$ and 4° for 0.133 and 600 s, respectively; (middle, red) those same angles collected for 0.133 and 60 s; and (bottom, green) a single measurement at 2.5° collected for 60 s. The datasets are offset by a factor of 100 from each other.

captured in the dynamic range parameter D [Eq. (5)]. Among current instruments, INTER at ISIS (Webster *et al.*, 2006) and FIGARO at ILL (Campbell *et al.*, 2011) most resemble the FTS-LR (Ankner *et al.*, 2002) in scientific mission and performance. As part of an ongoing round-robin measurement and from personal experience (JFA), a conventional dataset may be collected on these instruments in an hour or so. Both INTER and FIGARO exhibit a larger dynamic range than the FTS-LR, comparable to that proposed for QIKR, enabling a range of interesting kinetic measurements (Campbell *et al.*, 2011). QIKR is designed as a next-generation version of these horizontal-surface reflectometers, featuring 15–30× faster data collection. Current measurements using the FTS-LR (Blair *et al.*, 2022), FIGARO (Yuen *et al.*, 2019), and INTER (Skoda *et al.*, 2017) achieve <30 s time resolution (Campbell, 2018), so collection of comparable datasets with <5 s time resolution over the full Q range at QIKR should be routine.

There are two instruments on the horizon promising comparable kinetic performance to that of QIKR. FREIA (FREIA, 2022), currently under construction at the European Spallation Source, will be a horizontal-surface time-of-flight reflectometer utilizing a sophisticated chopper system and fast switching between three incident beams to achieve data collection projected to be 25× faster than that of FIGARO. The CANDOR reflectometer (CANDOR, 2022), an inverse-geometry instrument in commissioning at NIST, will employ several white incident beams and an array of analyzer crystals to cover a broad Q range without employing time-of-flight. The novelty of the concept makes it difficult to assess performance, but it will be interesting to see how the instrument performs. For samples exhibiting negligible off-specular scattering, using an angularly divergent beam in combination with a wide bandwidth provides an alternative method for sub-second time-resolved measurements (Saerbeck *et al.*, 2018).

The coming decade will witness the deployment and ongoing worldwide use of a set of reflectometers of unprecedented kinetic capability (<1 s frame rates in favorable cases). Of these instruments, QIKR will possess the virtue of simplicity, being a throwback to first-generation reflectometers.

ACKNOWLEDGMENTS

This manuscript has been authored by UT-Battelle, LLC under Contract No. DE-AC05-00OR22725 with the U.S. Department of Energy. The United States Government retains and the publisher, by accepting the article for publication, acknowledges that the United States Government retains a nonexclusive, paid-up, irrevocable, worldwide license to publish or reproduce the published form of this manuscript or allow others to do so, for United States Government purposes. The Department of Energy will provide public access to these results of federally sponsored research in accordance with the DOE Public Access Plan (http://energy.gov/downloads/doe-public-access-plan). G.M.V. was supported by the U.S. Department of Energy's Office of Basic Energy Sciences, Division of Materials Science and Engineering.

AUTHOR DECLARATIONS

Conflict of Interest

The authors have no conflicts to disclose.

Author Contributions

J. F. Ankner: Conceptualization (lead); Writing – original draft (lead). **R. Ashkar**: Writing – original draft (supporting). **J. F. Browning**: Conceptualization (supporting). **T. R. Charlton**: Conceptualization (supporting). **M. Doucet**: Conceptualization (supporting); Software (equal). **C. E. Halbert**: Conceptualization (supporting). **F. Islam**: Software (supporting). **A. Karim**: Conceptualization (supporting). **E. Kharlampieva**: Writing – original draft (supporting). **S. M. Kilbey II**: Writing – original draft (supporting). **J. Y. Y. Lin**: Software (equal). **M. D. Phan**: Conceptualization (supporting); Writing – original draft (supporting). **G. S. Smith**: Conceptualization (supporting); Writing – original draft (supporting). **S. A. Sukhishvili**: Writing – original draft (supporting). **R. Thermer**: Conceptualization (supporting). **G. M. Veith**: Writing – original draft (supporting). **E. B. Watkins**: Writing – original draft (supporting); Writing – review & editing (supporting). **D. Wilson**: Conceptualization (supporting).

DATA AVAILABILITY

The data that support the findings of this study are available from the corresponding author upon reasonable request.

APPENDIX: TWO-SLIT ACCEPTANCE

The concept of acceptance may be illustrated by considering the transmission of neutrons between two absorbing apertures (Fig. 19). The set of all possible trajectories through the slits is bounded by extreme trajectories, two of which are shown in green. These trajectories and the area they bound are plotted in Fig. 20 for $s_d = 0.159$ cm; $s_u = 0.968$ cm; $l_{ud} = 190$ cm. The labeled vertices define a polygon containing all allowed trajectories plotted as the height, y, the neutron crosses the downstream slit vs the angular deviation, $\boldsymbol{\gamma}_y$, of the path from the centerline. The labeled vertices are the extreme paths through the two slits: (1) bottom–top (upward ray in Fig. 19); (2) bottom–bottom; (3) top–bottom (downward ray in Fig. 19); and (4) top–top. Approximating trigonometric functions to first order, the coordinates of these vertices are, respectively,

$$[(s_u + s_d)/2l_{ud}, s_d/2], \tag{A1}$$

$$[(s_u - s_d)/2l_{ud}, -s_d/2], \tag{A2}$$

$$[-(s_u + s_d)/2l_{ud}, -s_d/2], \tag{A3}$$

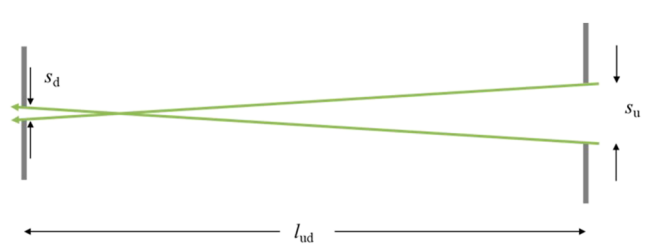

FIG. 19. Dimensions of two absorbing apertures and the top–bottom and bottom–top extreme neutron paths through them (green).

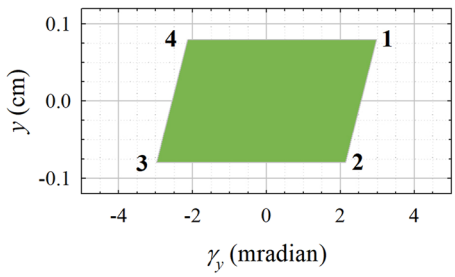

FIG. 20. Acceptance diagram plotting aperture vs angular deviation from the centerline for neutron passage through the slits shown in Fig. 19 (s_d = 0.159 cm, s_u = 0.968 cm, and l_{ud} = 190 cm). The bounding trajectories are (1) bottom–top (upward ray in Fig. 19); (2) bottom–bottom; (3) top–bottom (downward ray in Fig. 19); and (4) top–top. All possible trajectories are found within the green parallelogram.

$$[-(s_u - s_d)/2l_{ud}, s_d/2]. \tag{A4}$$

After passage through the slits, this population of neutrons ballistically traverses a distance l_{ds} = 10 cm to the sample—their angular trajectories do not change (neglecting gravity over the short distance l_{ds}) but the beam spreads out in space (Fig. 21). The population of allowed trajectories may now be described by the "sheared" polygon (Carpenter and Mildner, 1982) depicted in Fig. 22 bounded by the vertices,

$$[(s_u + s_d)/2l_{ud}, s_d/2 + l_{ds}(s_u + s_d)/2l_{ud}], \tag{A5}$$

$$[(s_u - s_d)/2l_{ud}, -s_d/2 + l_{ds}(s_u - s_d)/2l_{ud}], \tag{A6}$$

$$[-(s_u + s_d)/2l_{ud}, -s_d/2 - l_{ds}(s_u + s_d)/2l_{ud}], \tag{A7}$$

$$[-(s_u - s_d)/2l_{ud}, s_d/2 - l_{ds}(s_u - s_d)/2l_{ud}]. \tag{A8}$$

We can investigate the angular distribution of the neutrons incident onto the sample by integrating the acceptance diagram over the spatial coordinate y,

$$\text{rocking curve} \equiv \int_{-s_s/2}^{s_s/2} A_y(y, \gamma_y)\,dy. \tag{A9}$$

Recall from Eq. (7) that A_y is the vertical acceptance of the optics. The integral of the distribution over the spatial coordinate

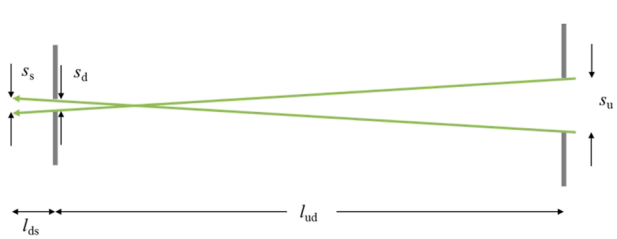

FIG. 21. Ballistic extension of the rays in Fig. 19 a distance l_{ds} to the sample, where the rays are now a distance s_s apart.

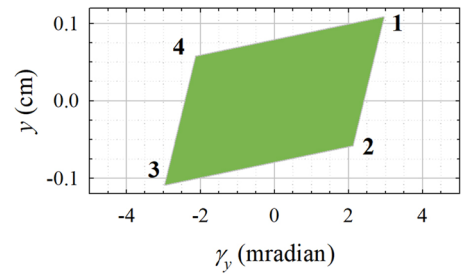

FIG. 22. "Sheared" acceptance diagram of the neutron population shown in Fig. 20 after traveling a distance l_{ds} = 10 cm to the sample.

shown in Fig. 22 is plotted in Fig. 23. We can determine the full width at half maximum (fwhm) of this rocking curve using the angular coordinates in Eqs. (A5)–(A8) labeled for the vertices in Figs. 22 and 23,

$$\delta\gamma_{fwhm} = \frac{1}{2}(\gamma_1 + \gamma_2) - \frac{1}{2}(\gamma_3 + \gamma_4) \approx \frac{s_u}{l_{ud}}. \tag{A10}$$

Direct this neutron beam onto a sample at an angle θ, assuming for simplicity that we are measuring in the θ–θ geometry. Then, $\delta\theta \equiv \delta\gamma_{fwhm}$ and note from Fig. 22 that the spatial extent of the beam is $s_s = y_1 - y_3$. The extent of the beam footprint on the sample (F) depicted in Fig. 10 in the main text can thus be linked to the dimensions of the incident beam,

$$F \sin\theta \approx F\theta = s_s = y_1 - y_3 = s_d + \frac{l_{ds}(s_u + s_d)}{2l_{ud}}. \tag{A11}$$

Solve Eq. (A11) for θ and use the expression for beam divergence in Eq. (A10) to obtain

$$\frac{\delta\theta}{\theta} = \frac{Fs_u}{l_{ud}s_d + l_{ds}(s_u + s_d)}. \tag{A12}$$

The upstream slit opening expression given in Eq. (8) in the main text then follows from plugging Eq. (A12) into Eq. (A10) and solving for s_u. Then, substitute that expression into Eq. (A11) and solve for s_d to get Eq. (9). The acceptance integrated over both spatial and angular coordinates in Eq. (10) is just the area of the polygon in Fig. 22 (or in Fig. 20 since no neutrons are lost between slits and

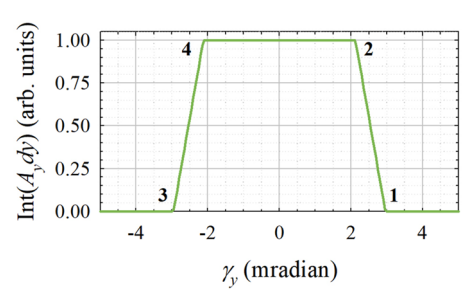

FIG. 23. Acceptance distribution from Fig. 22 integrated over the spatial coordinate and normalized to the peak value.

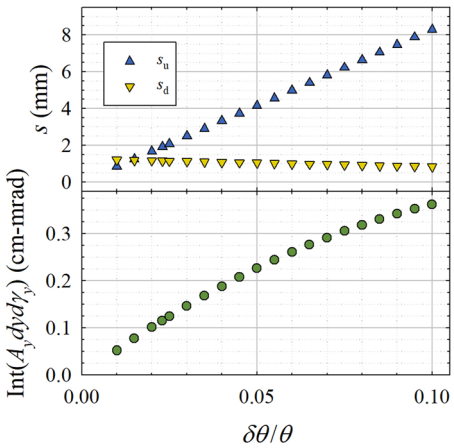

FIG. 24. (Top) Required apertures upstream (s_u) and downstream (s_d) for a beam incident onto a sample at θ_i = 2.5° painting an F = 3 cm footprint when l_{ud} = 190 cm and l_{ds} = 10 cm at different values of relative angular resolution $\delta\theta/\theta$ per Eqs. (8) and (9) in the main text. (Bottom) Integrated acceptance for those slit settings per Eq. (10) in the main text.

sample). As shown in Fig. 24, neutron counts (proportional to integrated acceptance) (bottom) can be traded for coarser resolution by opening the upstream aperture s_u and mildly throttling the downstream aperture s_d to maintain a constant footprint F as described by Eqs. (8)–(10). It is straightforward to modify these expressions for small samples, where the footprint cannot be practically confined to the sample surface. In this case, the sample serves as the downstream aperture and one replaces s_d by $F \sin\theta$ and l_{ud} by $l_{ud} + l_{ds}$.

REFERENCES

Ankner, J. F. and Felcher, G. P., "Polarized neutron reflectometry," J. Magn. Magn. Mater. **200**, 741–754 (1999).

Ankner, J. F. and Majkrzak, C. F., "Subsurface profile refinement for neutron specular reflectivity," Proc. SPIE **1738**, 260–269 (1992).

Ankner, J. F., Rehm, C., Blakeman, E. D., and Kellogg, R. L., "Optical design of the SNS liquids reflectometer," Proc SPIE **4785**, 53–63 (2002).

Ashkar, R., Bilheux, H. Z., Bordallo, H., Briber, R., Callaway, D. J. E., Cheng, X., Chu, X.-Q., Curtis, J. E., Dadmun, M., Fenimore, P., Fushman, D., Gabel, F., Gupta, K., Herberle, F., Heinrich, F., Hong, L., Katsaras, J., Kelman, Z., Kharlampieva, E., Kneller, G. R., Kovalevsky, A., Krueger, S., Langan, P., Lieberman, R., Liu, Y., Lösche, M., Lyman, E., Mao, Y., Marino, J., Mattos, C., Meilleur, F., Moody, P., Nickels, J. D., O'Dell, W. B., O'Neill, H., Perez-Salas, U., Peters, J., Petridis, L., Sokolov, A. P., Stanley, C., Wagner, N., Weinrich, M., Weiss, K., Wymore, T., Zhang, Y., and Smith, J. C., "Neutron scattering in the biological sciences: Progress and prospects," Acta Crystallogr., Sect. D: Struct. Biol. **74**(12), 1129–1168 (2018).

Auth, T., Dasgupta, S., and Gompper, G., "Interaction of particles and pathogens with biological membranes," in *Physics of Biological Membranes*, edited by Bassereau, P. and Sens, P. (Springer International Publishing, Cham, 2018), pp. 471–498.

Avdeev, M. V., Rulev, A. A., Bodnarchuk, V. I., Ushakova, E. E., Petrenko, V. I., Gapon, I. V., Tomchuk, O. V., Matveev, V. A., Pleshanov, N. K., Kataev, E. Y., Yashina, L. V., and Itkis, D. M., "Monitoring of lithium plating by neutron reflectometry," Appl. Surf. Sci. **424**, 378–382 (2017).

Benedetto, A., Heinrich, F., Gonzalez, M. A., Fragneto, G., Watkins, E., and Ballone, P., "Structure and stability of phospholipid bilayers hydrated by a room-temperature ionic liquid/water solution: A neutron reflectometry study," J. Phys. Chem. B **118**(42), 12192–12206 (2014).

BES, Energy Storage Grand Challenge Roadmap, U.S. Department of Energy, 2020; accessed via https://www.energy.gov/energy-storage-grand-challenge/downloads/energy-storage-grand-challenge-roadmap, August 2, 2022.

Bi, J., Wang, R., and Zeng, X., "Lipid rafts regulate the lamellipodia formation of melanoma A375 cells via actin cytoskeleton-mediated recruitment of β1 and β3 integrin," Oncol. Lett. **16**(5), 6540–6546 (2018).

Blair, S. J., Doucet, M., Browning, J. F., Stone, K., Wang, H., Halbert, C., Avilés Acosta, J., Zamora Zeledón, J. A., Nielander, A. C., Gallo, A., and Jaramillo, T. F., "Lithium-mediated electrochemical nitrogen reduction: Tracking electrode–electrolyte interfaces via time-resolved neutron reflectometry," ACS Energy Lett. **7**, 1939–1946 (2022).

Bongomin, F., Gago, S., Oladele, R., and Denning, D., "Global and multi-national prevalence of fungal diseases-estimate precision," J. Fungi **3**(4), 57 (2017).

Born, M. and Wolf, E., *Principles of Optics*, 6th ed. (Pergamon, New York, 1980).

Browning, K. L., Browning, J. F., Doucet, M., Yamada, N. L., Liu, G., and Veith, G. M., "Role of conductive binder to direct solid–electrolyte interphase formation over silicon anodes," Phys. Chem. Chem. Phys. **21**(31), 17356–17365 (2019).

Browning, K. L., Sacci, R. L., Doucet, M., Browning, J. F., Kim, J. R., and Veith, G. M., "The study of the binder poly(acrylic acid) and its role in concomitant solid–electrolyte interphase formation on Si anodes," ACS Appl. Mater. Interfaces **12**(8), 10018–10030 (2020).

Campbell, R. A., "Recent advances in resolving kinetic and dynamic processes at the air/water interface using specular neutron reflectometry," Curr. Opin. Colloid Interface Sci. **37**, 49–60 (2018).

Campbell, R. A., Wacklin, H. P., Sutton, I., Cubitt, R., and Fragneto, G., "FIGARO: The new horizontal neutron reflectometer at the ILL," Eur. Phys. J. Plus **126**, 107 (2011).

CANDOR, CHRNS CANDOR–White-Beam Reflectometer; accessed at https://www.nist.gov/ncnr/chrns-candor-white-beam-reflectometer, August 16, 2022.

Carpenter, J. M. and Mildner, D. F. R., "Neutron guide tube gain for a remote finite source," Nucl. Instrum. Methods Phys. Res., Sect. A **196**, 341–348 (1982).

Chi, E. Y., Krishnan, S., Randolph, T. W., and Carpenter, J. F., "Physical stability of proteins in aqueous solution: Mechanism and driving forces in nonnative protein aggregation," Pharm. Res. **20**, 1325–1336 (2003).

Cohen-Tannoudji, C., Diu, B., and Laloë, F., *Quantum Mechanics* (Wiley, New York, 1977), Vol. I.

DeCaluwe, S. C., Dhar, B. M., Huang, L., He, Y., Yang, K., Owejan, J. P., Zhao, Y., Talin, A. A., Dura, J. A., and Wang, H., "Pore collapse and regrowth in silicon electrodes for rechargeable batteries," Phys. Chem. Chem. Phys. **17**(17), 11301–11312 (2015).

de Lange, E. C. M., "Multi drug resistance P glycoprotein and other transporters," in *Encyclopedia of Stress*, 2nd ed., edited by Fink, G. (Academic Press, New York, 2007), pp. 774–783.

Dorrell, M. W., Heberle, F. A., Katsaras, J., Maibaum, L., Lyman, E., and Sodt, A. J., "Laterally resolved small-angle scattering intensity from lipid bilayer simulations: An exact and a limited-range treatment," J. Chem. Theory Comput. **16**(8), 5287–5300 (2020).

Dyson, H. J. and Wright, P. E., "Coupling of folding and binding for unstructured proteins," Curr. Opin. Struct. Biol. **12**, 54–60 (2002).

EBRC, Engineering Biology and Materials Science: A Research Roadmap for Interdisciplinary Innovation, found at https://roadmap.ebrc.org/2021-roadmap-materials/; accessed August 3, 2022.

Egrot, A. P. G., Marquette, C. A., and Blum, L. J., "Biomimetic membranes and biomolecule immobilisation strategies for nanobiotechnology applications," Int. J. Nanotechnol. **7**, 753–780 (2010).

Fears, T. M., Doucet, M., Browning, J. F., Baldwin, J. K. S., Winiarz, J. G., Kaiser, H., Taub, H., Sacci, R. L., and Veith, G. M., "Evaluating the solid electrolyte interphase formed on silicon electrodes: A comparison of *ex situ* X-ray photoelectron spectroscopy and *in situ* neutron reflectometry," Phys. Chem. Chem. Phys. **18**(20), 13927–13940 (2016).

Felcher, G. P., Hilleke, R. O., Crawford, R. K., Haumann, J., Kleb, R., and Ostrowski, G., "Polarized neutron reflectometer: A new instrument to measure magnetic depth profiles," Rev. Sci. Instrum. **58**, 609–619 (1987).

Felici, R., Penfold, J., Ward, R. C., and Williams, W. G., "A polarised neutron reflectometer for studying surface magnetism," Appl. Phys. A **45**, 169–174 (1988).

Fragneto-Cusani, G., "Neutron reflectivity at the solid/liquid interface: Examples of applications in biophysics," J. Phys.: Condens. Matter **13**, 4973–4989 (2001).

FREIA, FREIA Liquids Reflectometer; accessed at https://europeanspallationsource.se/instruments/freia#instrument-description, August 16, 2022.

Gallmeier, F. X., Lu, W., Riemer, B. W., Zhao, J. K., Herwig, K. W., and Robertson, J. L., "Conceptual moderator studies for the Spallation Neutron Source short-pulse second target station," Rev. Sci. Instrum. **87**, 063304 (2016).

Gerelli, Y., Porcar, L., and Fragneto, G., "Lipid rearrangement in DSPC/DMPC bilayers: A neutron reflectometry study," Langmuir **28**(45), 15922–15928 (2012).

Geyer, F., D'Acunzi, M., Sharifi-Aghili, A., Saal, A., Gao, N., Kaltbeitzel, A., Sloot, T.-F., Berger, R., Butt, H.-J., and Vollmer, D., "When and how self-cleaning of superhydrophobic surfaces works," Sci. Adv. **6**, eaaw9727 (2020).

Gropp, R. E., "NSF: Time for big ideas," BioScience **66**, 920 (2016).

Hirayama, M., Yonemura, M., Suzuki, K., Torikai, N., Smith, H., Watkinsand, E., Majewski, J., and Kanno, R., "Surface characterization of $LiFePO_4$ epitaxial thin films by X-ray/neutron reflectometry," Electrochemistry **78**(5), 413 (2010).

Hemminger, J. C. (chair), "Challenges at the frontiers of matter and energy: Transformative opportunities for discovery science," A Report from the Basic Energy Sciences Advisory Committee, U.S. Department of Energy, 2015, available at https://science.osti.gov/-/media/bes/besac/pdf/Reports/Challenges_at_the_Frontiers_of_Matter_and_Energy_rpt.pdf; accessed, August 3, 2022.

Hoogerheide, D. P., Noskov, S. Y., Jacobs, D., Bergdoll, L., Silin, V., Worcester, D. L., Abramson, J., Nanda, H., Rostovtseva, T. K., and Bezrukov, S. M., "Structural features and lipid binding domain of tubulin on biomimetic mitochondrial membranes," Proc. Natl. Acad. Sci. U. S. A. **114**(18), E3622–E3631 (2017).

Jerliu, B., Dörrer, L., Hüger, E., Borchardt, G., Steitz, R., Geckle, U., Oberst, V., Bruns, M., Schneider, O., and Schmidt, H., "Neutron reflectometry studies on the lithiation of amorphous silicon electrodes in lithium-ion batteries," Phys. Chem. Chem. Phys. **15**(20), 7777–7784 (2013).

Jerliu, B., Hüger, E., Dörrer, L., Seidlhofer, B.-K., Steitz, R., Oberst, V., Geckle, U., Bruns, M., and Schmidt, H., "Volume expansion during lithiation of amorphous silicon thin film electrodes studied by *in-operando* neutron reflectometry," J. Phys. Chem. C **118**(18), 9395–9399 (2014).

Junghans, A., Watkins, E. B., Barker, R. D., Singh, S., Waltman, M. J., Smith, H. L., Pocivavsek, L., and Majewski, J., "Analysis of biosurfaces by neutron reflectometry: From simple to complex interfaces," Biointerphases **10**(1), 019014 (2015).

Kawaura, H., Harada, M., Kondo, Y., Mizutani, M., Takahashi, N., and Yamada, N. L., "*Operando* time-slicing neutron reflectometry measurements of solid electrolyte interphase formation on amorphous carbon surfaces of a Li-ion battery," Bull. Chem. Soc. Jpn. **93**(7), 854–861 (2020).

Klein, A. G. and Werner, S. A., "Neutron optics," Rep. Prog. Phys. **46**, 259–335 (1983).

Levental, I., Levental, K. R., and Heberle, F. A., "Lipid rafts: Controversies resolved, mysteries remain," Trends Cell Biol. **30**(5), 341–353 (2020).

Lin, J. Y. Y., Islam, F., Sala, G., Lumsden, I., Smith, H., Doucet, M., Stone, M. B., Abernathy, D. L., Ehlers, G., Ankner, J. F., and Granroth, G. E., "Recent developments of MCViNE and its applications at SNS," J. Phys. Commun. **3**, 085005 (2019).

Liscovitch, M. and Lavie, Y., "Multidrug resistance: A role for cholesterol efflux pathways?," Trends Biochem. Sci. **25**(11), 530–534 (2000).

Luchini, A., Gerelli, Y., Fragneto, G., Nylander, T., Pálsson, G. K., Appavou, M.-S., and Paduano, L., "Neutron reflectometry reveals the interaction between functionalized SPIONs and the surface of lipid bilayers," Colloids Surf., B **151** 76–87 (2017).

Maan, A. M. C., Hofman, A. H., Vos, W. M., and Kamperman, M., "Recent developments and practical feasibility of polymer-based antifouling coatings," Adv. Funct. Mater. **30**, 2000936 (2020).

Majewski, J., Kuhl, T. L., Wong, J. Y., and Smith, G. S., "X-ray and neutron surface scattering for studying lipid/polymer assemblies at the air–liquid and solid–liquid interfaces," Rev. Mol. Biotechnol. **74**(3), 207–231 (2000).

Majkrzak, C. F., Berk, N. F., Krueger, S., Dura, J. A., Tarek, M., Tobias, D., Silin, V., Meuse, C. W., Woodward, J., and Plant, A. L., "First-principles determination of hybrid bilayer membrane structure by phase-sensitive neutron reflectometry," Biophys. J. **79**(6), 3330–3340 (2000).

McCluskey, A. R., Grant, J., Smith, A. J., Rawle, J. L., Barlow, D. J., Lawrence, M. J., Parker, S. C., and Edler, K. J., "Assessing molecular simulation for the analysis of lipid monolayer reflectometry," J. Phys. Commun. **3**(7), 075001 (2019).

Michel, V. and Bakovic, M., "Lipid rafts in health and disease," Biol. Cell **99**(3), 129–140 (2007).

Minato, T., Kawaura, H., Hirayama, M., Taminato, S., Suzuki, K., Yamada, N. L., Sugaya, H., Yamamoto, K., Nakanishi, K., Orikasa, Y., Tanida, H., Kanno, R., Arai, H., Uchimoto, Y., and Ogumi, Z., "Dynamic behavior at the interface between lithium cobalt oxide and an organic electrolyte monitored by neutron reflectivity measurements," J. Phys. Chem. C **120**(36), 20082–20088 (2016).

NAE, National Academy of Engineering Grand Challenges for Engineering, available at http://www.engineeringchallenges.org/challenges.aspx; accessed August 2, 2022.

Nanda, H., Datta, S. A. K., Heinrich, F., Lösche, M., Rein, A., Krueger, S., and Curtis, J. E., "Electrostatic interactions and binding orientation of HIV-1 matrix studied by neutron reflectivity," Biophys. J. **99**(8), 2516–2524 (2010).

Nash, K. L., in *Separations for the Nuclear Fuel Cycle in the 21st Century*, ACS Symposium Series Vol. 933, edited by Lumetta, G. J., Nash, K. L., Clark, S. B., and Friese, J. I. (American Chemical Society, Washington, DC, 2006), pp. 21–40.

Nielsen, C. H., "Biomimetic membranes for sensor and separation applications," Anal. Bioanal. Chem. **395**(3), 697–718 (2009).

NSF, NSF's 10 Big Ideas, available at https://www.nsf.gov/news/special_reports/big_ideas/index.jsp; accessed August 2, 2022.

ORNL, "First experiments: New science opportunities at the Spallation Neutron Source Second Target Station," Oak Ridge National Laboratory Technical Report No. SPR-2019/1407 TRN: US2216148, 2019, available at https://neutrons.ornl.gov/sites/default/files/STS_First_Experiments_Report.pdf; accessed August 2, 2022.

Parratt, L. G., "Surface studies of solids by total reflection of X-rays," Phys. Rev. **95**, 359–369 (1954).

Peetla, C., Stine, A., and Labhasetwar, V., "Biophysical interactions with model lipid membranes: Applications in drug discovery and drug delivery," Mol. Pharm. **6**(5), 1264–1276 (2009).

Peled, E., "The electrochemical behavior of alkali and alkaline earth metals in nonaqueous battery systems—The solid electrolyte interphase model," J. Electrochem. Soc. **126**(12), 2047–2051 (1979).

Peled, E. and Menkin, S., "Review—SEI: Past, present and future," J. Electrochem. Soc. **164**(7), A1703–A1719 (2017).

Phan, M. D., Korotych, O. I., Brady, N. G., Davis, M. M., Satija, S. K., Ankner, J. F., and Bruce, B. D., "X-ray and neutron reflectivity studies of styrene-maleic acid copolymer interactions with galactolipid-containing monolayers," Langmuir **36**, 3970–3980 (2020).

Rockwell, N. C., "Multidrug resistance membrane proteins," in *Encyclopedia of Biological Chemistry*, 2nd ed., edited by Lennarz, W. J. and Lane, M. D. (Academic Press, Waltham, MA, 2013), pp. 210–214.

Saerbeck, T., Cubitt, R., Wildes, A., Manzin, G., Andersen, K. H., and Gutfreund, P., "Recent upgrades of the neutron reflectometer D17 at ILL," J. Appl. Crystallogr. **51**, 249–256 (2018).

Sanchez, I. C., *Physics of Polymer Surfaces and Interfaces* (Butterworth-Heinemann, Waltham, MA, 2013).

Schlossman, M. L., "Liquid-liquid interfaces: Studied by X-ray and neutron scattering," Curr. Opin. Colloid Interface Sci. **7**, 235–243 (2002).

Sears, V. F., "Neutron scattering lengths and cross sections," Neutron News **3**(3), 26–37 (1992).

Seidlhofer, B.-K., Jerliu, B., Trapp, M., Hüger, E., Risse, S., Cubitt, R., Schmidt, H., Steitz, R., and Ballauff, M., "Lithiation of crystalline silicon as analyzed by operando neutron reflectivity," ACS Nano **10**(8), 7458–7466 (2016).

Shipman, G., Campbell, S., Dillow, D., Doucet, M., Kohl, J., Granroth, G., Miller, R., Stansberry, D., Proffen, T., and Taylor, R., "Accelerating data acquisition, reduction, and analysis at the spallation neutron source," in *2014 IEEE 10th International Conference on e-Science* (IEEE, 2014), pp. 223–230.

Simons, K. and Ikonen, E., "Functional rafts in cell membranes," Nature **387**, 569–572 (1997).

Singhal, T., "A review of coronavirus disease-2019 (COVID-19)," Indian J. Pediatr. **87**(4), 281–286 (2020).

Siontorou, C., Nikoleli, G.-P., Nikolelis, D., and Karapetis, S., "Artificial lipid membranes: Past, present, and future," Membranes **7**(3), 38 (2017).

Skoda, M. W. A., Thomas, B., Hagreen, M., Sebastiani, F., and Pfrang, C., "Simultaneous neutron reflectometry and infrared reflection absorption spectroscopy (IRRAS) study of mixed monolayer reactions at the air–water interface," RSC Adv. **7**, 34208–34214 (2017).

Squires, G. L., *Introduction to the Theory of Thermal Neutron Scattering*, 3rd ed. (Cambridge University Press, Cambridge, 2012).

Stockton, W. B. and Rubner, M. F., "Molecular-level processing of conjugated polymers. 4. Layer-by-layer manipulation of polyaniline via hydrogen-bonding interactions," Macromolecules **30**, 2717–2725 (1997).

Sun, X., Daoud, M., Farnoux, B., and Jannink, G., "Concentration gradient near the surface of a polymer," Physica B **156–157**, 407–409 (1989).

SwissNeutronics, See https://www.swissneutronics.ch/products/neutron-supermirrors/, viewed August 15, 2022.

Tasker, P. A. *et al.*, in *Comprehensive Coordination Chemistry II: From Biology to Nanotechnology*, edited by McCleverty, J. A. and Meyer, T. J. (Elsevier, Oxford, 2004), pp. 759–808.

Veith, G. M., Baggetto, L., Sacci, R. L., Unocic, R. R., Tenhaeff, W. E., and Browning, J. F., "Direct measurement of the chemical reactivity of silicon electrodes with $LiPF_6$-based battery electrolytes," Chem. Commun. **50**(23), 3081–3084 (2014).

Veith, G. M., Doucet, M., Baldwin, J. K., Sacci, R. L., Fears, T. M., Wang, Y., and Browning, J. F., "Direct determination of solid-electrolyte interphase thickness and composition as a function of state of charge on a silicon anode," J. Phys. Chem. C **119**(35), 20339–20349 (2015).

Veith, G. M., Doucet, M., Sacci, R. L., Vacaliuc, B., Baldwin, J. K., and Browning, J. F., "Determination of the solid electrolyte interphase structure grown on a silicon electrode using a fluoroethylene carbonate additive," Sci. Rep. **7**(1), 6326 (2017).

Verma, P., Maire, P., and Novák, P., "A review of the features and analyses of the solid electrolyte interphase in Li-ion batteries," Electrochim. Acta **55**(22), 6332–6341 (2010).

Webster, J., Holt, S., and Dalgliesh, R., "INTER the chemical interfaces reflectometer on target station 2 at ISIS," Physica B **385–386**, 1164–1166 (2006).

Willendrup, P. K. and Lefmann, K., J. Neutron Res. **22**(1), 1–16 (2020).

Willendrup, P. K. and Lefmann, K., J. Neutron Res. **23**(1), 7–27 (2021).

Wong, J. Y., Majewski, J., Seitz, M., Park, C. K., Israelachvili, J. N., and Smith, G. S., "Polymer-cushioned bilayers. I. A structural study of various preparation methods using neutron reflectometry," Biophys. J. **77**(3), 1445–1457 (1999).

Yan, H., Wu, Q., Yu, C., Zhao, T., and Liu, M., "Recent progress of biomimetic antifouling surfaces in marine," Adv. Mater. Interfaces **7**, 2000966 (2020).

Yingchoncharoen, P., Kalinowski, D. S., and Richardson, D. R., "Lipid-based drug delivery systems in cancer therapy: What is available and what is yet to come," Pharmacol. Rev. **68**(3), 701–787 (2016).

Young-Rok, K., Sungho, J., Huunil, R., Yeong-Eun, Y., Sun Min, K., and Tae-Joon, T., "Synthetic biomimetic membranes and their sensor applications," Sensors **12**(7), 9530–9550 (2012).

Yuen, F., Watson, M., Barker, R., Grillo, I., Heenan, R. K., Tunnacliffe, A., and Routh, A. F., "Preferential adsorption to air–water interfaces: A novel cryoprotective mechanism for LEA proteins," Biochem. J. **476**, 1121–1135 (2019).

Zhang, X., Brodus, D., Hollimon, V., and Hu, H., "A brief review of recent developments in the designs that prevent bio-fouling on silicon and silicon-based materials," Chem. Cent. J. **11**, 18 (2017).

Zhao, J. K., Robertson, J. L., Herwig, K. W., Gallmeier, F. X., and Riemer, B. W., "Optimizing moderator dimensions for neutron scattering at the spallation neutron source," Rev. Sci. Instrum. **84**, 125104 (2013).